

Wall emission in circumbinary disks: the case of CoKu Tau/4

Erick Nagel^{1,2}, Paola D'Alessio¹, Nuria Calvet³, Catherine Espaillat^{4,5}, Ben Sargent⁶, Jesús Hernández⁷, and William J. Forrest⁸

Centro de Radioastronomía y Astrofísica, UNAM, Morelia, Michoacán, México 58089

Departamento de Astronomía, Universidad de Guanajuato, Guanajuato, Gto, México 36240

Department of Astronomy, University of Michigan, Ann Arbor, MI 48109

Harvard-Smithsonian Center for Astrophysics, 60 Garden Street, MS-78, Cambridge, MA, 02138

NSF Astronomy & Astrophysics Postdoctoral Fellow

Space Telescope Science Institute, Baltimore, MD 21218

Centro de Investigaciones de Astronomía, Mérida 5101-A, Venezuela

Department of Physics and Astronomy, University of Rochester, Rochester, NY 14627

erick@astro.ugto.mx

ABSTRACT

A few years ago, the mid-IR spectrum of a Weak Line T Tauri Star, CoKu Tau/4, was explained as emission from the inner wall of a *circumstellar* disk, with the inner disk truncated at ~ 10 AU. Based on the SED shape and the assumption that it was produced by a single star and its disk, CoKu Tau/4 was classified as a prototypical transitional disk, with a clean inner hole possibly carved out by a planet, some other orbiting body, or by photodissociation. However, recently it has been discovered that CoKu Tau/4 is a close binary system. This implies that the observed mid-IR SED is probably produced by the *circumbinary* disk. The aim of the present paper is to model the SED of CoKu Tau/4 as arising from the inner wall of a circumbinary disk, with parameters constrained by what is known about the central stars and by a dynamical model for the interaction between these stars and their surrounding disk. We lack a physical prescription for the shape of the wall, thus, here we use a simplified and unrealistic assumption: the wall is vertical. In order to fit the Spitzer IRS SED, the binary orbit should

be almost circular, implying a small mid-IR variability (10 %) related to the variable distances of the stars to the inner wall of the circumbinary disk. In the context of the present model, higher eccentricities would imply that the stars are farther from the wall, the latter being too cold to explain the observed SED. Our models suggest that the inner wall of CoKu Tau/4 is located at $1.7a$, where a is the semi-major axis of the binary system ($a \sim 8AU$). A small amount of optically thin dust in the hole ($\lesssim 0.01$ lunar masses) helps to improve the fit to the $10 \mu\text{m}$ silicate band. Also, we find that water ice should be absent or have a very small abundance (a dust to gas mass ratio $\lesssim 5.6 \times 10^{-5}$). In general, for a binary system with eccentricity $e > 0$, the model predicts mid-IR variability with periods similar to orbital timescales, assuming that thermal equilibrium is reached instantaneously.

Subject headings: circumstellar matter – infrared: stars – stars:pre-main-sequence

1. Introduction

Until recently, the Weak Line T Tauri star, CoKu Tau/4 (Cohen & Kuhi 1979), was known as a remarkable example of a transitional disk (Forrest et al. 2004). Its mid-IR SED (IRS Spitzer) was modeled by D’Alessio et al. (2005), hereafter D05, taking an isolated star, and they concluded that the disk surrounding CoKu Tau/4 should have a clean inner hole, with a radius about 10 AU. In this model, the emergent flux in the mid-IR spectral range was produced by the inner wall of the truncated disk.

Previously, it had been thought that the inner hole of CoKu Tau/4 was due to either a recently formed planet (Quillen et al. 2004) or by the UV switch model (Clarke et al. 2001; Alexander & Armitage 2007) due to its undetectable accretion signatures. However, observations described by Ireland & Kraus (2008) show conclusively that CoKu Tau/4 is a binary system, implying that its inner hole is probably produced by dynamical interactions between the binary system and the surrounding gas.

For a binary system formed by stars of similar masses and using the predictions of Artymowicz & Lubow (1994) and Beust & Dutrey (2005), Ireland & Kraus (2008) estimated that the size of the hole in the circumbinary disk (CB hereafter) should be between 13 and 16 AU, for different eccentricities of the binary orbits. The estimated hole is larger than the one found in the D05 transitional disk model, and being further away, one would naively expect it to be cooler. However, the stars are not at the geometrical center of the disk: each point in the visible part of the wall is at a different distance from the stars. Therefore,

the net effect of both stars in the heating of the wall should be calculated for a particular configuration before comparison with the observed SED.

This paper has several goals. The first is to find a simplified structure of the inner edge of the CB disk around the CoKu Tau/4 binary system that consistently reproduces the observed spectral energy distribution (SED). The second is to determine the properties of the dust particles of that edge. Spitzer observations probe mostly the upper layers of the inner 10-20 AU regions of typical disks (D’Alessio et al. 2006), while at the present resolution of submillimeter and millimeter interferometers, the main contribution comes from the midplane at larger distances. In contrast, circumbinary and transitional disks are truncated at a certain radius, making them a natural laboratory to study the dust near the midplane in the inner disk region, inaccessible by other means. In § 2 we describe the physics of the models, and in § 3 we present the fiducial model adopted as a reference for later comparisons; in § 4 we study the effects of changing parameters in the SED of the fiducial model; in § 5 we apply our methods to the case of CoKu Tau/4, and in § 6 we discuss our results and give conclusions.

2. Description of the model

Our basic model consists of a CB disk, from which only its inner wall contributes to the SED in the mid-IR spectral range ($5 - 40\mu\text{m}$), surrounding two stars that contribute mainly to the near-IR flux. The main difference between the present model and the one described in D05 is that here the inner wall is irradiated by two stars and each of them has a different distance to any surface element of the wall since neither of the stars is located at the geometrical center of the CB disk. Moreover, since the stars are moving in their orbits, their distance to each portion of the inner wall changes with time. Assuming that the wall reaches thermal equilibrium in a timescale shorter than the orbital timescale of the binary system (see the Appendix for the evaluation of this assumption), the temperature of each portion of the wall and the resulting SED are periodically variable with its orbital timescale.

The fact that we are describing a CB disk implies that a whole set of new parameters should be included into the model, in comparison to the model proposed by D05. At first sight, it might look like this increasing degree of freedom makes the problem degenerate. However, new restrictions allow one to break part of this degeneracy, as we will see in the following sections.

Figure 1 shows the geometrical parameters that describe the spatial configuration of the system, namely, the semi-major axis a , eccentricity e and the angle ϕ , that locates one of

the stars in an elliptical orbit with the other one at the focus. Figure 1 shows the two angles that are required to characterize this configuration in 3D space: i , the inclination between the disk axis and the line of sight (or, between the disk plane and the plane of the sky) and α , which gives the axis in the disk plane around which the disk is inclined. This line passes through the center of the elliptical orbit and the angle α is measured between this line and the major axis line. Note that first the system is described in the orbital plane with a , e and ϕ (see Figure 1). Then, the major axis line is identified, from which an angle α gives the line around which the system is inclined an angle i . An inclined system is shown in Figure 2. For these parameters, the origin of the reference system is in the center of the ellipse. Notice that changing α not only changes the orientation of the visible part of the wall, but also modifies the distances from the stars to that part of the wall (§ 2.1). On the other hand, a variation in i changes the visible area of the wall (§ 2.1). In the following, the angles ϕ and α are given in units of π radians.

The inner wall or inner boundary of the CB disk is characterized by its radius R_{cb} , and its vertical height, h . Notice that in this system of reference, while the second star describes the elliptical orbit, the center of mass of the binary system and also the center of the hole in the CB disk move (both points are the same for $e = 0$ but not for other values of eccentricity, e.g., Pichardo et al. (2005) and Pichardo et al. (2008)). Thus, during a binary system orbit, the distance between the two stars and the wall changes. For the following, the origin of our system of reference is the center of the CB disk.

Also, it is important to specify the dust composition of the material in the hot atmosphere of the wall. We assume that, in general, the dust is a mixture of silicates, troilite, graphite, amorphous carbon and water ice. The silicate (olivine or pyroxene) and graphite abundances are given by Draine & Lee (1984). The maximum abundance of water ice and the abundance of troilite is taken from Pollack et al. (1994). We change the dust composition and abundances in § 4 and adjust them by comparing the synthetic and the observed SEDs in § 5.

A constraint inherent to a two-star model is given by the dynamical interaction of the binary system with a disk. This interaction clears an inner hole, thus, in this way the radius R_{cb} is determined by the stars' masses and the eccentricity and semi-major axis of their orbits. In contrast, in the case of one star (D05) R_{wall} is a free parameter. In order to reproduce the observed SED, R_{wall} was adjusted to obtain the appropriate temperature structure.

The size of the hole (R_{cb}) can be calculated numerically (Rudak & Paczynski (1981), Pichardo et al. (2005), Pichardo et al. (2008), Artymowicz & Lubow (1994)) or analytically for a circular binary (Nagel et al. 2008). However, Artymowicz & Lubow (1994) take a

hydrodynamical approach with the inclusion of viscosity, in addition to the gravitational interaction of the stars and the disk material. The presence of viscosity allows the material to move to the region where there are no stable orbits around both stars. If a mass particle passes a certain point, then the only possibility for it is to move to one of the stars. In this way, streams of material originating in the CB disk connect to the circumstellar disks (these are disks inside the hole surrounding each star), acting as a feeding mechanism (Artymowicz & Lubow 1996; Günther & Kley 2002). Observations by Jensen et al. (2007) suggest the presence of streams from the CB disk towards the binary system UZ Tau E. Also, for the binary St 34, Hartmann et al. (2005) argue that the presence of dust in the dynamically cleared hole is consistent with having some accretion flow onto the central binary. Günther et al. (2004), described the emission of DQ Tau and AK Sco using a hydrodynamical simulation, where all the disks and the streams connecting them are taken into account. Also, binaries of very low mass are expected to be fed by a circumbinary disk (Robberto et al. 2008). From all these studies, we can argue that the truncation radius R_{cb} strongly depends on the viscosity in a non trivial way. For an $e > 0$ system, Artymowicz & Lubow (1994) show clear differences between R_{cb} for changes in the Reynolds number, which depends on the viscosity. However, in order to take a more realistic model, we decided to use the results of Artymowicz & Lubow (1994) taken from Figure 3, arguing that R_{cb} does not depend strongly on the stars mass ratio, and a Reynolds number of 10^4 .

An important ingredient for the calculation of the radiation flux from the stars impinging on the circumbinary wall is the distance between each star and a specific point on the wall, $R_{1,2}$ (see Figures 1 and 2). In order to calculate these distances, the first step is to give the locations of the stars in the configuration where one star is at the focus and the other is on a point on its corresponding ellipse. The second step is to place a circular CB disk with its origin at the point corresponding to the eccentricity of the binary system (see Pichardo et al. 2005, 2008), e.g., the center of mass of the binary system if $e = 0$, with a radius given by Artymowicz & Lubow (1994). Finally, the third step is to calculate the distances between the coordinates of the stars and each surface element of the wall given in this reference system (see Figures 1 and 2).

2.1. Formulation of the wall emission problem

The inner wall of the CB disk is assumed to be vertical, i.e., the vector normal to its surface is parallel to the disk midplane. In order to relax the assumption of verticality one requires a way to describe the shape of the wall, which is not possible to the best of our knowledge, because the observations and simulations do not have the necessary resolution.

More complicated shapes have been assumed for the dust to gas transition at the dust destruction radius in the inner disk by taking into account the dependence of the sublimation temperature or density (Isella & Natta 2005) or the maximum grain size (Tannirkulam et al. 2007). However, the edge of the CB disk is a physical wall created by tidal interactions with the binary system, and the vertical density profile may be very different from that in standard disks. Since no detailed models exist to guide us, we have adopted the simplest geometry: a vertical wall. The wall is also assumed to be circular for simplicity, however, non-axisymmetric shapes are expected based on hydrodynamical simulations of Günther & Kley (2002) and Artymowicz & Lubow (1996). In Section 4.1 we show that the SED for an eccentric CB disk does not change appreciably with respect to the circular case, thus the CoKu Tau/4 modeling is restricted to the latter.

Only a fraction of the wall’s surface can be detected by the observer, depending on the wall radius, height and the inclination angle i . There are other portions of the wall that are occulted from the observer by absorption due to the disk itself. The “visible” surface, projected in the plane of the sky (see Figure 2), is divided in small surface elements (pixels). Each one is located at a given height relative to the disk midplane, Y and at a given distance, X , from the disk center. In order to describe each pixel position, we use cartesian coordinates (see D05).

Each point in the wall has a different temperature distribution, from the surface toward larger radii (deeper inside the disk). In order to estimate this temperature distribution we use a similar treatment given by Calvet et al. (1991) and Calvet et al. (1992). However, in the present case each pixel is being irradiated by two stars, neither of which is at the center of the system. We use the fact that the luminosity from the wall is much less than the luminosity from the stars in order to neglect its contribution to the heating of the wall. Thus, at each pixel we consider the superposition of two radiation fields, characterized by two different fluxes and mean intensities, and, in principle, by two distinct incidence directions. The incident flux from each star is $F_{0,j} = (L_{*,j}/4\pi R_j^2)\mu$ with each star at a different distance from the wall, given by R_j , μ is the cosine of the incidence angle with respect to the normal to the wall surface. Again, for the sake of simplicity, we assume that each pixel is a plane parallel atmosphere and the radiation from each star arrives in a single beam, with a normal incidence angle ($\mu = 1$). This assumption is valid only if the minimum distance between the stars and the wall is much larger than the stellar radii. In the case of CoKu Tau/4, the minimum distance between one star and the wall is $1.2 a \sim 9AU$, so the later assumption is justified for this particular object.

Following Calvet et al. (1991) and D05, the radiation field arriving at each pixel is then separated into three components: “stellar 1”, “stellar 2” and “disk”, each one with a

particular wavelength range where most of its emission peaks. Defining the optical depth at the “disk” wavelength range in the radial direction, measured from the wall surface towards larger radii, the net outward Eddington flux at the disk frequency range, H_d , is given by

$$H_d(\tau_d) = \sum_{j=1}^2 \frac{F_{0,j}}{4\pi} \alpha_1 [(1 + C_{1,j})e^{-q_j\tau_d} + C_{2,j}e^{-\beta_j q_j \tau_d}], \quad (1)$$

where α_j is the mean true absorption coefficient, $\kappa_{s,j}$, divided by the mean total disk opacity, χ_d (calculated including true absorptions and scattering), evaluated using the effective temperature of each star (given by $j = 1$ or 2), and $\beta_j = (3\alpha_j)^{1/2}$. Here, $q_j (= \chi_{s,j}/\chi_d)$, is the ratio between the mean total opacity at the stellar wavelength range and the mean total opacity at the disk range (which is the opacity used to calculate τ_d). The constants in equation (1) are given by equations 2 and 3 in D05, but in here they are evaluated using the mean opacities corresponding to each star.

All the mean opacities are calculated using the Planck function evaluated at the local or at the stellar effective temperature as the weighting function. The reason is that this kind of average is easy to calculate and the mean contributions of scattering and true absorption can be added together to give the total opacity, in contrast to a Rosseland kind of average (D’Alessio et al. 1998). Using this kind of mean opacity we obtain the correct value of temperature at $\tau_d \rightarrow 0$, because this is adequate for the optically thin layers of the wall atmosphere (Mihalas 1978).

The Eddington flux leads to the mean intensity at the disk frequency range, using the first momentum of the transfer equation and the usual boundary condition $J_d(0) = 2H_d(0)$.

From the zeroth moment of the transfer equation, assuming isotropic scattering, the temperature can be written as,

$$T(\tau_d)^4 = \sum_{j=1}^2 \alpha_j \frac{F_{0,j}}{4\sigma_R} (C'_{1,j} + C'_{2,j}e^{-q_j\tau_d} + C'_{3,j}e^{-\beta_j q_j \tau_d}), \quad (2)$$

with constants given in D05. Another, more compact, way to write down equation (2) is

$$T(\tau_d)^4 = T_1(\tau_d)^4 + T_2(\tau_d)^4, \quad (3)$$

where T_1 and T_2 are the temperatures calculated as if only the star 1 or 2 are present, respectively, as a superposition solution. However, in spite of its apparent simplicity, this

is really an implicit equation for the temperature since the mean opacities involved in the calculation of T_1 and T_2 depend on the temperature T .

As in Calvet et al. (1991), Calvet et al. (1992) and D05, we have assumed that the opacities are constant in the wall atmosphere, i.e., α_j and q_j are independent of τ_d . If the opacity is dominated by dust, and the temperature distribution in the wall atmosphere is such that there is no sublimation of any dust ingredient at a particular optical depth, then it is valid to assume that α_j is constant. Also, if the contrast in temperature between the uppermost and the deepest layers is not very high, χ_d and q_j can be assumed to be constant too. Thus, in order to quantify the mean opacities, we use the temperature evaluated at $\tau_d = 0$, i.e., the surface temperature T_{wall} . This is found solving the implicit equation (2), for a given wall radius R_{cb} , a given configuration of the binary system, and the coordinates of each pixel in the wall, a pair (X, Y) .

The monochromatic emergent intensity from each pixel of the wall in the direction of the observer is calculated by integrating the transfer equation. We consider two components: the thermal emission and the scattering of stellar radiation. Finally, the SED is calculated by multiplying the emergent intensity by the solid angle subtended by each (“visible”) pixel, as seen by the observer.

2.2. Formulation of the hole emission problem

As described in § 2, the size of the hole (R_{cb}) is given by the dynamical interaction between the disk and the stars. However, the full hydrodynamical treatment should include ingredients like the gas viscosity, that allows material from the CB disk to lose angular momentum and fall into the hole. This results in a small quantity of material inside the CB disk hole, that can be treated as being optically thin. Avoiding the precise description of the dynamical evolution of such particles, in this work we simplify the problem considering them distributed in a region located between a radius $R = R_{min}$ and $R = R_{cb}$, uniformly distributed in the azimuthal angle in a cylindrical coordinate system, centered at the center of mass of the binary system. Indeed, simulations of the material inside the hole (Artymowicz & Lubow 1996; Günther & Kley 2002) indicate that the material is non axisymmetric distributed and spans all radii less than R_{cb} . However, for a circular binary system with undetectable accretion towards the stars, we can argue that most of the material is restricted to lie at radius larger than the outer Lagrangian point for the three body circular restricted problem (Szebehely 1967). The surface density is given by a power law ($\Sigma \propto R^p, p = 1$) such that Σ increases closer to the wall, as is expected (Artymowicz & Lubow 1996).

The emergent flux from the dust in the hole depends on the dust temperature. Since we assume the hole is optically thin, then each dust grain is heated by absorption of geometrical diluted radiation from each star and cools down by emission of its own thermal radiation. This is expressed by the radiative equilibrium equation, written as

$$\int_0^\infty \kappa_\nu J_\nu^* d\nu = \int_0^\infty \kappa_\nu B_\nu(T(R, \theta)) d\nu, \quad (4)$$

where the mean intensity of the radiation field is approximated by

$$J_\nu^* \approx W_1(R_1, R_{*1})B_\nu(T_{*1}) + W_2(R_2, R_{*2})B_\nu(T_{*2}), \quad (5)$$

with the dilution factors,

$$W_j = \frac{1}{2} \left[1 - \sqrt{1 - \left(\frac{R_{*j}}{R_j} \right)^2} \right], \text{ for } j = 1, 2. \quad (6)$$

When the integrals are performed, the dust grain temperature is the solution of the implicit equation

$$T(R, \theta)^4 = \sum_{j=1}^2 W_j T_{*j}^4 [\kappa_{s,j} / \kappa_d(T(R, \theta))], \quad (7)$$

where $\kappa_d(T(R, \theta))$ is the Planck mean opacity given by

$$\kappa_d(T(R, \theta)) = \frac{\int_0^\infty \kappa_\nu(T) B_\nu(T) d\nu}{\sigma T^4 / \pi}, \quad (8)$$

and $\kappa_{s,j}(T(R, \theta), T_{*j})$ is a Planck-like mean opacity, which can be written as

$$\kappa_{s,j}(T(R, \theta), T_{*j}) = \frac{\int_0^\infty \kappa_\nu(T) B_\nu(T_{*j}) d\nu}{\sigma T_{*j}^4 / \pi}. \quad (9)$$

Here, we use the dust temperature to evaluate the monochromatic opacity and the stellar effective temperature (for each star, $j = 1$ or 2) to evaluate the Planck function in the average. The Planck-like mean opacity is the straightforward result from the solution of the radiative equilibrium equation.

The monochromatic opacities we use are calculated assuming a size distribution for the grains. In the present work, which is our first approximation to the problem, we do not calculate a particular temperature for each grain size, but a mean temperature for the whole size distribution. In this approximation, the emission is produced from small to large grains at the same temperature, however, for the full case, the emission from small and large grains will differ due to their different temperature. Thus, we assume that the differences in the emitted spectrum between the approximation and the real case are small. In § 4 we explore different ingredients for the dust in the hole.

3. Fiducial model

As described, this problem is too complex. Moreover, a full analysis of all the parameters involved is beyond our actual computational resources. Thus, we restrict the problem to variations around a fiducial model (E1 in table 2), where some parameters are fixed. Observations of the stellar parameters and orbital parameters help restrict the set of free parameters. Comparison between the synthetic and observed SED then provides a range for the rest of the parameters.

We adopt parameters relevant to CoKu Tau/4 for the fiducial model. First of all, the model requires the parameters that characterize the stars. What is assumed for the stars is mostly based on the observations reported by Ireland & Kraus (2008) for CoKu Tau/4. The masses of the stars ($M_{\star 1}$ and $M_{\star 2}$) have a ratio $M_{\star 2}/M_{\star 1} = 0.85 \pm 0.05$, and near-IR colors consistent with typical T Tauri spectral types. These stellar masses, combined with a , give the distance of each of the stars to the center of mass of the binary system. Also, assuming the stars are coeval, by specifying each of their masses, their ages and a stellar evolutionary model, one obtains the stellar radii ($R_{\star 1,2}$), their effective temperatures ($T_{\star 1,2}$) and their luminosities ($L_{\star 1,2}$).

In this paper we adopt the stellar evolutionary tracks from Siess et al. (2000), and the spectra are taken from synthetic stellar spectrum from libraries from A. Bruzual, which are described in Bruzual & Charlot (1993). For practical purposes, we take the sum of the spectra of two appropriate stars for comparison with the observed spectra at large frequencies. This process results in two spectral types for both stars. Ireland & Kraus (2008) propose the stars have $M1.5 \pm 0.5$ spectral types, consistent with an age of 4 *Myrs*. Here, we use the evolutionary tracks from Siess et al. (2000) given in $0.1M_{\odot}$ steps. Taking this restriction, we adopt *M0* and *M1* spectral type stars, which are within the uncertainties (A. Kraus, personal communication). Table 1 shows the parameters for the stars.

Figure 3 shows the stellar spectra for the binary stars with an age of 4 *Myrs*, corrected using $A_V = 3$ and four different extinction laws (Moneti et al. 2001; Draine 2003; McClure 2009; Mathis 1990). The spectra corrected with Draine (2003), Mathis (1990), and McClure (2009) are very close. Note that the extinction law in the near-IR does not introduce noticeable changes in the SED, but it affects the mid-IR spectral region (see Figure 3).

We note that from the spectrum there is no evidence of circumstellar disks, since the SED of CoKu Tau/4 at $\lambda \leq 8\mu m$ seems to be completely described by photospheric emission of the stars (Ireland & Kraus 2008). Moreover, CoKu Tau/4 is classified a WTTS, with an $H\alpha$ equivalent width consistent with negligible accretion from any possible circumstellar disks to the stars, with a rate constrained to be $\dot{M} < 10^{-12} M_\odot/\text{year}$, which is an observational threshold for accretion, according to Muzerolle et al. (2000). Thus, in the fiducial model we do not consider the presence of circumstellar disks.

We find that only a particular range in wall temperatures [$T_{wall}(X, Y, \tau_d)$] produces the observed SED consistent with the observed SED of CoKu Tau/4. T_{wall} strongly depends on the range of distances of the stars to all the points in the wall. As noted above, R_{cb} is no longer a free parameter and depends primarily on the eccentricity (e): if e increases, R_{cb} increases, too, and then both T_{wall} and F_{obs} decrease. For the fiducial model, we adopt the Artymowicz & Lubow (1994) value for R_{cb} ($= 1.7a$) for a $e = 0$ system for simplicity.

In order to fix α and ϕ , we consider configurations with the highest emergent flux. For this to be done, we need to search between configurations along the whole orbit of the system. However, the angle ϕ is irrelevant because the orbit is circular, but the angles α and i have to be specified. The former defines what fraction of the wall is directed towards the observer and the latter, the projection of the wall in the plane of the sky. The stars are not illuminating the wall homogeneously and there are two intensity peaks in the positions (X,Y) closest to each of the stars. The only configuration in which both intensity maxima are observed is the case where the stars are located in the axis around which the system is inclined, $\phi = 0.5$ and $\alpha = 0$. Thus, we choose this configuration in an effort to reduce the number of free parameters and to get a reasonable model to start with. This also turns out to be the highest flux model. For the same reason, we take the minimum observed semi-major axis ($a = 7.43AU$) as the fiducial value. As in D05, we choose $\cos i = 0.5$ as a typical value. In the fiducial model the height of the wall is assumed to be $h = 0.28a$.

Finally, for the fiducial model the dust composition consists of graphite, silicates, troilite and no water ice, with dust to gas mass ratios $\zeta_{grap} = 0.0025$ and $\zeta_{sil} = 0.0034$ (Draine & Lee 1984). The troilite abundance is $\zeta_{troi} = 7.68 \times 10^{-4}$ (Pollack et al. 1994). Graphite optical properties are taken from Weingartner & Draine (2001) for graphite, and the silicates are assumed to be pyroxenes ($Mg_{0.8}Fe_{0.2}SiO_3$), with optical properties from Dorschner et al.

(1995). Also, we consider an interstellar medium dust size distribution (Mathis et al. 1977) with $n(a) \propto a^{-3.5}$, with minimum and maximum sizes $a_{min} = 0.005\mu\text{m}$ and $a_{max} = 0.25\mu\text{m}$, respectively.

4. Effect of parameters on SED

To show the dependence of the SED on the input parameters we change one parameter at a time and compare the resultant SED to that of the fiducial model. We first consider the change of parameters in the wall, and then the change of parameters in the optically thin region inside the hole. We assume that the apparent separation of the stars on the plane of the sky is the same as the observed separation $d_{ap} = 53.6 \pm 0.5\text{mas} = 7.5 \pm 0.07\text{AU}$ (Ireland & Kraus 2008). This assumption implies a fixed semi-major axis, a . Note that the system configuration changes with time, thus, the d_{ap} will change, for a fixed a .

4.1. Effects of wall parameters on SED

In the modeling, the inner boundary of the CB disk is circular, which is the simplest assumption. However, in principle its shape can be non-axisymmetric. From the results of the hydrodynamical simulations of Artymowicz & Lubow (1996) and Günther & Kley (2002), we note that in the line that connects both stars, the disk material is approaching the outer lagrangian points. Thus, in order to quantify the difference between axisymmetric and non-axisymmetric models, we model the shape of the wall as an ellipse with its semiminor axis along this line. This is an easy way to get a non-axisymmetric wall, however, only a hydrodynamical simulation applied to systems like CoKu Tau/4 will allow us to accurately characterize the wall. Thus, the wall presented here is just one of many possibilities.

Figure 4 shows models with the parameters of the fiducial configuration, but with a semiminor axis for the CB disk of $b = R_{cb} - (0.4, 0.3, 0.2, 0.1, 0.0)a$. Note that the flux decreases for smaller b , which seems unphysical, due to the fact that the temperature of the wall closest to the stars is larger. However, the projected area perpendicular to the line of sight decreases in such a way that the second effect dominates the observed emission.

The main result is that the changes are restricted to wavelengths longer than $12\mu\text{m}$, thus, the silicates band is not modified. The changes are larger around $30\mu\text{m}$, but this is only relevant for smaller b , which represents a highly eccentric disk. This example shows how an elliptical wall modifies the SED, however, only when observations and/or simulations solve the structure of the wall, we will be able to quantify this effect in the modeling of CoKu

Tau/4.

Now, we consider changes of the binary system eccentricity, e , for $\phi = 0.5, \alpha = 0$, $\cos i = 0.5$ and $h = 0.28a$. Figure 5 shows the SED of the fiducial model and of models with $e = 0., 0.2, 0.4$, and 0.6 calculated with R_{cb} from Artymowicz & Lubow (1994). As e increases, so does R_{cb} . This figure shows that large values of e imply SEDs from colder walls, farther away from the stars, which show no $10 \mu m$ silicate feature. The wall surface temperature varies from $136.5 K$ for the smallest R_{cb} , and $80.7 K$ for the largest R_{cb} . In Table 2 we label these models as Series Ecc, where all the parameters are shown.

Figure 6 shows the effects of changing the angle α , for $\phi = 0.5, \cos i = 0.5, R_{cb} = 1.7a$ and $h = 0.28a$. Results are shown for $\alpha = 0, 0.25, 0.5, 1.5, 1.75$. In order to see the differences in terms of e , we show results for $e = 0$ and $e = 0.2$. For symmetry arguments (with respect to the $\phi = 0$ axis), the configurations for $\alpha = 0.75$ and 1.25 correspond to the same flux. The same can be said, for the $\alpha = 0.25$ and 1.75 cases. Moreover, the flux for all these cases is similar because the stars' masses are not so different and the binary orbit is circular. The configurations for $\alpha = 0$ and 1 correspond to the same flux, thus, the latter is not shown. The minimum flux is given in the $\alpha = 0.5$ model, where the disk is inclined around a line perpendicular to the line that connects both stars, for $\alpha = 0.5$ and $\alpha = 1.5$ the $10 \mu m$ band disappears. The maximum flux occurs in the $\alpha = 0$ model (or $\alpha = 1$). Changing α does not modify the area of the emitting region, since it only rotates this region in the plane of the sky. However, since the stars are not at the center of the wall, when α changes the distances of both stars to the visible area of the wall also change, and thus the resulting SED changes. We can conclude from Figure 6 that the cases are divided in two classes. The first one does not have a $10 \mu m$ band and the second one has this feature. These models, where α changes, for cases $e = 0$ and $e = 2$ are shown in Table 2 as Series α , ecc.

Figure 7 shows the SED when i and h varies, for $e = 0, \phi = 0.5, \alpha = 0$, and $R_{cb} = 1.7a$. The left plot corresponds to $h = 0.28a$ and $\cos i = 0.3, 0.5, 0.7$, and the right one is for $\cos i = 0.5$ and $h = 0.14, 0.28, 0.56$. The SED depends weakly on i , but, it has a strong dependence on h , namely, the flux increases for larger h . The reason for the former, is that for a perfectly vertical wall, the flux does not change monotonically with i . Of course, this effect will change if a realistic shape of the wall is taken. However, at this moment there are no studies (as far as we know) which define this shape (see Section 6), thus, we assume a vertical wall. Also, we are ignoring possible oscillation modes in the wall (Hayasaki & Okazaki 2009) due to the tidal potential of the binary. If the disk is viewed pole-on there is no visible area. In the opposite case, the emission from the wall of a disk seen edge-on is completely extinguished by the disk itself. Thus, the range in $\cos i$ relevant for modeling is small and the variation can be neglected. In the present model, the height of the wall is taken as an

arbitrary free parameter that can be adjusted to compensate for any variation of i . Models showing changes in i and h are presented in Table 2 as Series i, h .

A complete analysis of all the possibilities that describe the dust composition of the wall is computationally demanding, so we decided to explore the changes on the SED for typical cases. All these models can be used as a starting point to tackle future mid-IR spectra modeling with observations of new binary targets.

Figure 8 shows the effect on the SED of changing the type of silicates, for $e = 0, \phi = 0.5, \alpha = 0, \cos i = 0.5, R_{cb} = 1.7a$ and $h = 0.28a$. We show results for the fiducial model, and for the case where the silicates component are changed from pyroxenes ($Mg_{0.8}Fe_{0.2}SiO_3$) to olivines ($MgFeSiO_4$), model PO1 in Table 2 and the only member of Series pyr,oliv. The flux from the wall is larger when the dust is made by olivines (model P01) than when it is made by pyroxenes (fiducial model). This can be explained, because the former model has a higher temperature at the same distance from the central star. Another difference is that the central wavelength of the $10\mu\text{m}$ feature due to olivines is slightly shifted to longer wavelengths than the feature for the pyroxenes.

Figure 9 shows the effect on the SED of changing the type of carbon, for $e = 0, \phi = 0.5, \alpha = 0, \cos i = 0.5, R_{cb} = 1.7a$ and $h = 0.28a$. We show results for the case where we take amorphous carbon (Mathis & Whiffen 1989) and graphite (Weingartner & Draine 2001) grains. First, we compare two cases: a model with no graphite nor amorphous carbon (i.e., only pyroxene grains in the wall, model PA1) and a model like the fiducial one, but where graphite has been replaced by amorphous carbon (model PA2). We can see that model PA1 has a lower flux than model PA2, due to a lower T_{wall} , as noted in Table 2. The presence of amorphous carbon in model PA2 results in a larger temperature. For the same abundances, the absorption coefficients for graphite and amorphous carbon are similar between 0.3 and 3 microns, with the graphite opacity slightly larger. Outside this interval, the amorphous carbon opacity is higher. Thus, changes in the SED (see Figure 9) are expected due to the differences in the opacity for both components.

Also in Figure 9, models with variations on the abundance of graphite and amorphous carbon are also analyzed, for $e = 0, \phi = 0.5, \alpha = 0, \cos i = 0.5, R_{cb} = 1.7a$ and $h = 0.28a$. Results are shown for the cases where there is no amorphous carbon and the graphite abundance is halved and doubled (models PA3 and PA4 in table 2). In another case, the graphite is replaced by amorphous carbon; model PA5 corresponds to half the adopted standard value for amorphous carbon abundance and PA6 to the doubled value. For graphite and amorphous carbon, the flux increases as ζ increases. Model PA1 has the lowest flux. Physically this implies that silicates alone are heated at a much lower temperatures than the fiducial model, for the adopted value of R_{cb} . All the PA models are assembled in Table 2 as Series

pyr,amorph.

Figure 10 shows the effect on the SED of changing the water ice abundance, for $e = 0, \phi = 0.5, \alpha = 0, \cos i = 0.5, R_{cb} = 1.7a$ and $h = 0.28a$. The results are for four models, the water ice to gas mass ratios are $\zeta_{ice} = 0.0056$ (model PI4, abundance proposed by Pollack et al. (1994) for accretion disks), 50% (model PI3), 10% (model PI2) and 1% (model PI1) of the Pollack et al. value. These models are labeled in Table 2 as Series pyr,ice. We also use optical properties for crystalline water ice given by Warren (1984). We can see that for the two higher values of ice abundances, the $10\mu\text{m}$ feature disappears. The 10% case distorts this band significantly. Thus, for only 1% of this abundance, the SED is similar to our fiducial model. As we see in § 5 and § 6, this constrains the maximum allowed abundance of ice in the case of CoKu Tau/4. The wall temperature decreases as the ice abundance increases, thus, the presence of the $10\mu\text{m}$ band critically depends on T_{wall} .

Finally, Figure 11 shows the effect on the SED at different times, for $\alpha = 0, \cos i = 0.5$, and $h = 0.28a$. The results are shown for the evolution of the fiducial model in half an orbit, for times $t = \phi \times T/2 = (0, 0.25, 0.5, 0.75, 1.0) \times T/2$, where T is the orbital period. The maximum variation in the spectra occurs between $t = 0$ and $t = T/2$. In order to complete the orbit, the sequence of plots must be followed in inverse order. As expected, a circular binary system inside a circular CB disk shows small changes, within 10 %. Also in Figure 11, the time variation for an $e = 0.2$ system is shown. The results presented are for $t = (0, 0.2, 0.45, 0.7, 0.9) \times T/2$. When the stars are along a line perpendicular to the major axis, the wall emits its largest observable flux. The spread in fluxes is great given that in an eccentric system, the distances between the stars and the wall differ widely along the orbit. All these cases are placed under the name Series t,ecc in Table 2.

4.2. Effects of dust in the hole

Figure 12 shows the differences in the shape of the SED produced by the material within the hole. We present different values for the exponent of the mass surface density, $p = 0, 2, 10$, in the case of $e = 0$. In this example, the optically thin material is assumed to be between $R = R_{min} = 1.4a$ and $R_{cb} = 1.7a$ and is composed of $1 \times 10^{-9} M_{\odot}$ of pyroxene or olivine.

The emission of material highly concentrated in the wall ($p = 10$) is smaller than for the flatter density distributions ($p = 0$ and $p = 2$) for each type of silicates. Also, there is considerably more emission for the hole filled with olivines than for the hole filled by pyroxenes. The other noteworthy difference is that in the case of olivines, a $10\mu\text{m}$ band is

more conspicuous in the SED than for pyroxenes. The reason for all this is that, for the same system configuration, the olivines temperature is larger than the pyroxenes' temperature. In addition, the band for olivine peaks at a longer wavelength ($0.5\mu\text{m}$ greater) than the pyroxene band, making it look more like a peak since this wavelength is in the Wien's law side of the planck function.

Figure 13 shows the effect on the SED of changing R_{min} , the inner boundary of material in the hole. We show results for 3 cases: $R_{min} = 1.0a$, $R_{min} = 1.2a$ and $R_{min} = 1.4a$. As expected, the flux is larger for the smaller value for R_{min} , for which the material lies in a larger region of the hole.

Figure 14 shows the effect on the SED for different abundances of silicates. The results are for the case where graphite is included with the fiducial model abundance ($\zeta_{grap} = 0.0025$, Draine & Lee (1984)). The three studied cases are the standard value taken from Draine & Lee (1984) ($\zeta_{sil} = 0.0034$) as well as half and twice this value. Note that diminishing ζ_{sil} does not imply that the flux is smaller at all wavelengths because the opacity decreases, but the dust temperature increases. Changing ζ_{sil} and keeping ζ_{grap} constant means that we are changing the total dust to gas mass ratio and also the relative abundances of silicate and graphite. In this case both the fluxes and the shape of the SED change. On the other hand, since the emission emerges from an optically thin region, changing the dust to gas mass ratio while keeping the relative abundances of each ingredient constant, will make the shape of the SED remain the same. In this case, the fluxes will scale proportionally with the dust mass inside the hole. Thus, the inferred dust mass is sensitive to the dust properties and composition.

5. Application to the SED of CoKu Tau/4

The fiducial model was made using the known properties of CoKu Tau/4, and the geometrical restrictions given by the dynamical interaction between the binary system and the disk (Pichardo et al. 2005, 2008; Artymowicz & Lubow 1994). For the latter issue, note that the D05 models required a wall radius between 9 and $12AU$. For instance, $e = 0.8$, $R_{cb} \approx 3.5a$ (Pichardo et al. 2005), and $a \sim 8 AU$ (Ireland & Kraus 2008) implies $R_{cb} \sim 28 AU$, i.e., three times the required value in D05. Even for $e = 0$, Pichardo et al. (2005) find $R_{cb} \approx 1.9a$, giving $R_{cb} \sim 15 AU$, still too big for the implicitly required temperatures to explain the observed SED. However, including the disk viscosity, Artymowicz & Lubow (1994) find that for $e = 0$, $R_{cb} \approx 1.7a$, which corresponds to $\sim 13.5 AU$, still larger, but much closer to the wall radius estimated in D05. In this section, we show that the value for R_{cb} given in Artymowicz & Lubow (1994) results in a model of CoKu Tau/4, that fits the

observed SED, as shown in Figure 15.

In Figure 5 one can see that for $e > 0$ the wall is too cold, because the $10\mu\text{m}$ band does not match the observations. Even in some cases there is no band at $10\mu\text{m}$. Thus, a nearly circular binary orbit seems to be more consistent with the observed SED. We present a model, for a 4 *Myrs* system (model M1 in table 2) in Figure 15 for CoKu Tau/4 (labeled Series CoKu Tau/4), where only the parameters of the wall are presented. Indeed, this corresponds to the fiducial model (model E1) but here it is repeated for clarity.

The spectral types and masses of the stars consistent with the observed spectrum at high frequencies are $M1$ and $0.5M_{\odot}$ and $M0$ and $0.6M_{\odot}$, respectively. The spectrum corrected using the Draine’s law is better fitted by pyroxene dust grains. The higher wall temperature when olivines are used produces a flux larger than observed. Figure 3 presents the observations dereddened with Draine (2003), Mathis (1990), McClure (2009) and Moneti et al. (2001) laws. The flux for the observations dereddened with the Moneti et al. (2001) law is larger than that using the Draine (2003) law, the latter being taken here. Thus, olivine is a good option for modeling CoKu Tau/4, when using the Moneti law. A change in h can also increase the flux, but the depth of the $10\mu\text{m}$ feature changes (see Figure 7). The spectrum dereddened with the McClure (2009) law using $A_V = 2.5$ is indistinguishable from the data dereddened with Draine’s law and $A_V = 3$. Thus, the model presented here can be used for both cases. We use $h = 0.28a$ ($h = 0.15R_{cb}$) as a free parameter adjusted to fit the observed SEDs, but in the future it would be good to have an estimated range of h consistent with hydrodynamical arguments. Also, the wall cannot have a larger abundance of water ice ($\zeta_{ice} > 5.6 \times 10^5$); otherwise, it would change the shape of the $10\mu\text{m}$ observed band, as described in § 4.1 and shown in Figure 10. From Figure 9 one can conclude that amorphous carbon instead of graphite does not help to improve the fit, because the resulting $10\mu\text{m}$ band does not match the observed SED.

In the case of CoKu Tau/4, there is no evidence for circumstellar disks; thus, only a very small amount of mass should be able to cross the inner boundary of the CB disk. But even so, it could be enough material to produce a contribution to the mid-IR SED. Our wall emission model for CoKu Tau/4 shown in Figure 15 seems to produce a reasonable fit to the observed SED. This fit can be improved if optically thin material in the hole should be included. The fiducial model requires more flux at the right side of the $10\mu\text{m}$ band. Thus, looking at the inner hole emission models in § 4.2, we choose the one with $p = 1$, $R_{min} = 1.4a$ and pyroxenes dust grains (see Figure 12). A model with a lower R_{min} or with graphite has a prominent band at $10\mu\text{m}$, which implies a contribution at both sides of the fiducial model band, which is not what is needed in this case. The surface density profile is characterized by an exponent $p = 1$ (see § 2.2). The total mass in dust in this region is 0.006 lunar masses. The importance

of this final fit is that the optically thin material lies outside the Lagrangian point radius (R_{L_2}), i.e. the particles are located in a dynamically allowed region. Some of these particles will be able to accrete onto the stars due to viscosity effects (Artymowicz & Lubow 1994, 1996) or due to a not well-determined interior boundary (R_{min}). However, even if this mass is accreted, and a standard dust-to-gas mass ratio is assumed, the mass accretion rate onto the stars is below the observational threshold, $\dot{M} < 10^{-12} M_{\odot}/year$ (Muzerolle et al. 2000).

Figure 15 shows the model with and without material in the hole and the contribution from the optically thin material. Thus, the best-fit model to the emission of CoKu Tau/4 is the fiducial model, plus optically thin material distributed inside a geometrically thin ring close to the inner circumbinary wall.

6. Conclusions

We found a model that explains the observed mid-IR SED of CoKu Tau/4. The model has a binary system in a nearly circular orbit with 4 *Myrs* stars old (using the evolutionary tracks from Siess et al. (2000)) and a circumbinary disk truncated at $R_{cb} = 1.7a \sim 12.6$ AU, with $a = 7.43$ AU. The height of the inner wall of the CB disk is around $h/a \sim 0.3$, for $i = 60^\circ$. Also, we find that the inner hole might have a very small amount of dust ($\lesssim 0.006$ lunar masses) with a spatial distribution in agreement with dynamical arguments of the binary-disk interaction (see Artymowicz & Lubow (1994), Pichardo et al. (2005) and Pichardo et al. (2008)). A detailed study of the amount and distribution of mass in the hole, can give us information about the viscously driven process that allows for some particles to fall into the hole when losing angular momentum. This phenomenon strongly depends on h and α (viscosity coefficient from α -disk models, Shakura & Sunyaev (1973)), thus such a study can indirectly characterize these parameters. The model for the optically thin material in the hole can be used for arbitrary distributions of material in order to study the streams. The structure of the streams can be taken from the hydrodynamical simulations in Günther & Kley (2002) and Günther et al. (2004). However, in this preliminary study we adopt an axisymmetric dust distribution which might represent some kind of average of these streams' models. We leave a more detailed approach for future work.

Being a binary in a circular orbit, we predict a small variability ($\sim 10\%$) of the SED of CoKu Tau/4 in half its orbital timescale (~ 10 years), related to the changing distances between the stars and the CB disk. Other sources of variability are not accounted for in the present model. This prediction can be tested if observations at other times are available for this or other binary systems. On the other hand, if the binary orbit is not circular we found that no model can explain the observed SED because the inner wall of the CB disk is too

far away from the stars to have the appropriate temperature.

The study of the inner wall and the constraints on the dust sizes and abundances allows us to probe the dust even at the midplane, which is where planets must form. Note that Spitzer is sensitive to the dust located in the atmosphere of typical disks, not for matter in the midplane. The wall can be seen as a perpendicular cut through the disk. Thus, the details of the vertical structure are clearly exposed. In particular, the midplane is the place where material accumulates by settling. Eventually, the mass in this region is above the gravitational instability threshold (Goldreich & Ward 1973), and planetesimals are able to form (Youdin & Shu 2002). Thus, the study of this region is of prime importance. The advent of ALMA will allow us to actually see the wall. The current interferometers are able to get a resolution of $1''$, and at distances of typical regions of star formation, that means resolutions $\sim 15AU$. ALMA will have five times better resolution (Guilloteau & Dutrey 2008), thus the region of optically thin material inside the wall and the location of the wall can be resolved. The images produced can give us hints of the planetesimal formation process which will result in a complementary study to the disk structure analysis as the one presented here. Thus, studies of circumbinary and transitional disks, in particular the analysis of grain growth and settling in the wall, can place these disks in an evolutionary scheme. The dust composition can be traced since the formation process of the star+disk system, (due to the fact that much of the crystallization, just to name one process, occurs in the first stages of the formation, Dullemond et al. (2006)), until the phase of very evolved stars (Gielen et al. 2007). The connection between evolved stars and the current solar system is seen in binaries like AC Her and RU Cen. The infrared emission from the CB post-AGB disk shows a strong resemblance to the spectrum of the solar system primitive comet Hale-Bopp (Gielen et al. 2007). Thus, studies of dust emission of the inner part of the CB disk are important to improve our understanding of the bridge between young and old disks, from the formation of the disk to the formation of a planetary system.

In general, the model is not restricted to any configuration nor any particular combination of stars, so it could be applied and tested with other observed binaries with circumbinary disks. It is clear that observations with high resolution, like the ones described by Ireland & Kraus (2008), in which both stars can be characterized, are very useful. In the near future, other binary systems observed with Spitzer: Hen 3-600 (Uchida et al. 2004), St 34 (Hartmann et al. 2005), HD 98800 (Furlan et al. 2007), will be studied with this model. For these cases, the assumption was made that the binary can be approximated as an equivalent star with the luminosity of both. However, the results that come from this work, argue that this approximation should be taken with care. Finally, a more detailed wall structure can be adopted, as the inner curved rim described by Isella & Natta (2005) or Tannirkulam et al. (2007). In these works, the hole was formed by dust sublimation and the shape of the wall

was given in the former by a density dependent sublimation of grains, and in the latter by the vertical differentiation of grain sizes. In the case of a circumbinary disk, it is not so clear what the shape of the disk inner wall would be, but one expects that dynamical effects of the stars, hydrodynamical instabilities, pressure, viscosity or even evaporation of the disk due to radiation from the stars, will have a major role in the final shape of the wall. The relevance of the unrealistic assumption of a vertical wall is not the aim of this work, however a full characterization requires a detailed analysis, which is beyond the scope of this paper, and will be addressed in a following paper.

This work is based on observations made with the *Spitzer Space Telescope*, which is operated by the Jet Propulsion Laboratory, California Institute of Technology, under contract with NASA. We are indebted with Adam Kraus for the opportunity to exchange ideas with him. PD acknowledges a grant from CONACyT, México. EN appreciates postdoctoral fellowships from UNAM and CONACyT, México. CE was supported by the National Science Foundation under Award No. 0901947.

A. APPENDIX

The cooling/heating time is:

$$t_{c/h} = \frac{K\Sigma_R}{2\mu m_H \sigma T^3}, \quad (\text{A1})$$

where $\Sigma_R = \int_{R_{cb}}^{R_{cb}+dR} \rho dR$. Note that we are interested in the area parallel to the wall surface. The flux is equal to σT^4 , assuming blackbody emission at temperature T .

Now, a typical surface density for disks around T Tauri stars located at $10AU$ is $\Sigma_d \approx 10gcm^{-2}$ (D'Alessio et al. 1998), and the wall height in the fiducial model is $H = 0.28a = 3.34 \times 10^{13}cm$. Thus, an estimate for the volumetric density is

$$\rho = \frac{\Sigma_d}{H} \approx 3 \times 10^{-13}gcm^{-3}. \quad (\text{A2})$$

The emission from the wall is optically thick, such that the emission comes from a small radial region. In order to give an estimate for $t_{c/h}$, we take $\Delta R = H$, thus $\Sigma_R = \Sigma_d = 10gcm^{-2}$. For the temperature T , we take $T = \langle T_{wall} \rangle = 136.5K$, which corresponds to the fiducial model. Thus, the cooling/heating time is:

$$t_{c/h} \approx 2.86 \times 10^6 (\Sigma_R/10 \text{ g cm}^{-2}) (T_{\text{wall}}/135.6)^{-3} (\mu/1.)^{-1} \text{ s}. \quad (\text{A3})$$

The orbital time is simply

$$t_{\text{orb}} = \frac{a^{3/2}}{(G(M_{\star 1} + M_{\star 2}))^{1/2}} = 1.08 \times 10^8 \text{ s}. \quad (\text{A4})$$

We find that for typical parameters, $t_{c/h} \ll t_{\text{orb}}$, justifying the assumption of an instantaneous adjustment of the disk inner edge to changing stellar irradiation.

REFERENCES

- Alexander, R.D. & Armitage, P.J. 2007, MNRAS, 375, 500
- Artymowicz, P., & Lubow, S.H. 1994, ApJ, 421, 651
- Artymowicz, P., & Lubow, S.H. 1996, ApJ, 467, L77
- Beust, H., & Dutrey, A. 2005, A& A, 439, 585
- Bruzual, A.G., & Charlot, S. 1993, ApJ, 405, 538
- Calvet, N., Magris, G., Patiño, A., & D’Alessio, P. 1992, Rev. Mex. AA, 24, 27
- Calvet, N., Patiño, A., Magris, G., & D’Alessio, P. 1991, ApJ, 380, 617
- Clarke, C.J., Gendrin, A., & Sotomayor, M. 2001, MNRAS, 328, 485
- Cohen, M., & Kuhl, L.V. 1979, ApJS, 41, 743
- D’Alessio, P., Cantó, J., Calvet, N., & Lizano, S. 1998, ApJ, 500, 411
- D’Alessio, P. et al. 2005, ApJ, 621, 461 (D05)
- D’Alessio, P., Calvet, N., Hartmann, L., Franco-Hernández, R., & Servín, H. 2006, ApJ, 638, 314
- Dorschner, J., Begemann, B., Henning, T., Jäger, C., & Mutschke, H. 1995, A& A, 300, 503
- Draine, B.T. 2003, ARA& A, 41, 241
- Draine, B.T., & Lee, H.M. 1984, ApJ, 285, 89

- Dullemond, C.P., & Dominik, C. 2004, *A& A*, 421, 1075
- Dullemond, C.P., Apai, D., & Walch, S. 2006, *ApJ*, 640, L67
- Forrest, W.J. et al. 2004, *ApJS*, 154, 443
- Furlan, E. et al. 2007, *ApJ*, 664, 1176
- Gielen, C., van Winckel, H., Waters, L.B.F.M., Min, M., & Dominik, C. 2007, *A& A*, 475, 629
- Goldreich, P., & Ward, W.R. 1973, *ApJ*, 183, 1051
- Guilloteau, S., & Dutrey, A. 2008, *Astrophys.Space.Sci.*, 313, 95
- Guilloteau, S., Dutrey, A., Pety, J. & Gueth, F. 2008, *A& A*, 478, L31
- Günther, R., & Kley, W. 2002, *A& A*, 387, 550
- Günther, R., Schäfer, C., & Kley, W. 2004, *A& A*, 423, 559
- Hartmann, L. et al. 2005, *ApJ*, 628, L147
- Hayasaki, K., & Okazaki, A.T. 2009, *ApJL*, 691, L5
- Ireland, M.J., & Kraus, A.L. 2008, *ApJ*, 678, L59
- Isella, A. & Natta, A. 2005, *A& A*, 438, 899
- Jäger, C., Mutschke, H., Begemann, B., Dorschner, J., & Henning, T. 1994, *A& A*, 292, 641
- Jensen, E.L.N. et al. 2007, *AJ*, 134, 241
- Mathis, J.S., Rumpl, W., & Nordsieck, K.H. 1977, *ApJ*, 217, 425
- Mathis, J.S. 1990, *ARA& A*, 28, 37
- Mathis, J.S. & Whiffen, G. 1989, *ApJ*, 341, 808
- McClure, M. 2009, *ApJL*, 693, L81
- Mihalas, D. 1978, *Stellar Atmospheres* (2nd ed.; San Francisco: Freeman)
- Moneti, A., Stolovy, S., Blommaert, J.A.D.L., Figer, D.F., & Najarro, F. 2001, *A& A*, 366, 106
- Muzerolle, J., Calvet, N., Briceño, C., Hartmann, L., & Hillenbrand, L. 2000, *ApJ*, 535, L47

- Nagel, E., & Pichardo, B. 2008,MNRAS,384,548
- Pichardo, B.,Sparke, L.S., & Aguilar, L.A. 2005,MNRAS,359,521
- Pichardo, B.,Sparke, L.S., & Aguilar, L.A. 2008,MNRAS,391,815
- Pollack, J.B., Hollenbach, D., Beckwith, S., Simonelli, D.P.,Roush, T., & Fong, W. 1994,ApJ,421,615
- Quillen, A.C.,Blackman, E.G.,Frank, A., & Varnière, P. 2004,ApJ,612,L137
- Robberto, M., Ricci, L., Da Rio, N., & Soderblom, D.R. 2008,ApJ,687,L83
- Rudak, B., & Paczynski B. 1981,Acta Astron,31,13
- Shakura, N.I., & Sunyaev, R.A. 1973, A& A,24,337
- Siess, L.,Dufour, E., & Forestini, M. 2000,A& A,358,593
- Szebehely, V. 1967, Theory of orbits: the restricted problem of three bodies (Academic Press), pp.668
- Tannirkulam, A., Harries, T.J., & Monnier, J.D. 2007,ApJ,661,374
- Uchida, K.I. et al. 2004, ApJS, 154, 439
- Warren, S.G. 1984, Applied Optics, 23, 1206
- Weingartner, J.C., & Draine, B.T. 2001,ApJ,548,296
- Youdin, A.N., & Shu, F.H. 2002,ApJ,580,494

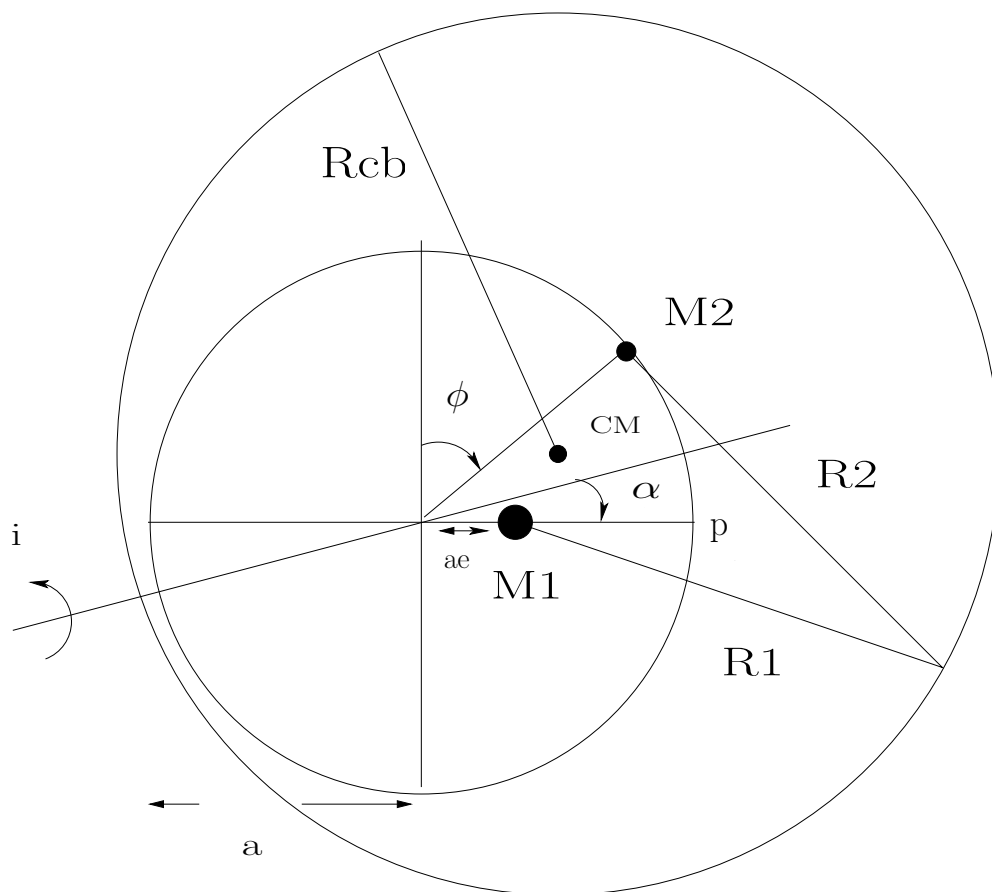


Fig. 1.— Schematic diagram of the parameters that characterizes the system configuration in space. The parameters shown are $M1, M2, R1, R2, R_{cb}, \alpha, \phi, i, a$ (see text for definitions), ae is the distance between the center of the ellipse and the star in the focus, p corresponds to the pericenter, the stars configuration of closest approach. The locations of the stars are given with respect to the center of the ellipse, and the center of the CB disk is given with respect to the center of mass (CM) of the binary system. The line given by the angle α is the one around which the system is inclined at an angle i . The figure is not to scale. See text for more details.

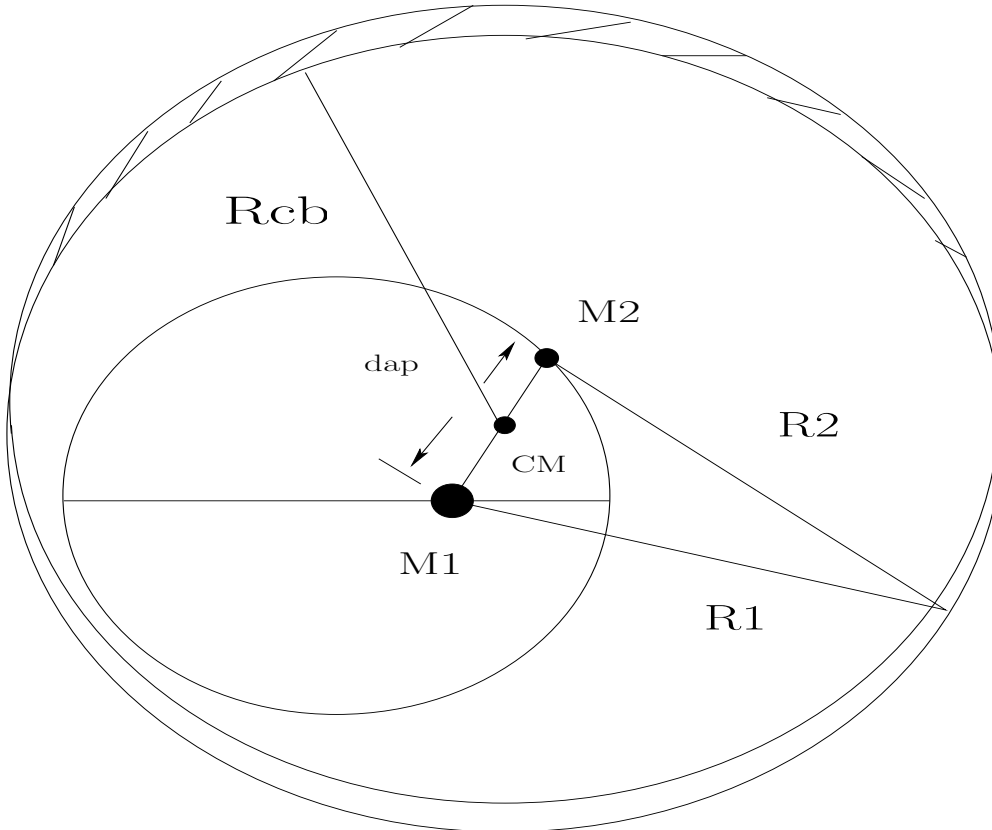


Fig. 2.— Schematic diagram of an inclined system with arbitrary i . In this example, the system is inclined around the major axis line, $\alpha = 0$. Here, d_{ap} corresponds to the distance between the stars in the plane of the sky. The dashed area shows the fraction of the wall directed towards the observer. The rest of the parameters are described in the text. The only difference between Figure 1 and this figure is that this one corresponds to an inclined system. The figure is not to scale.

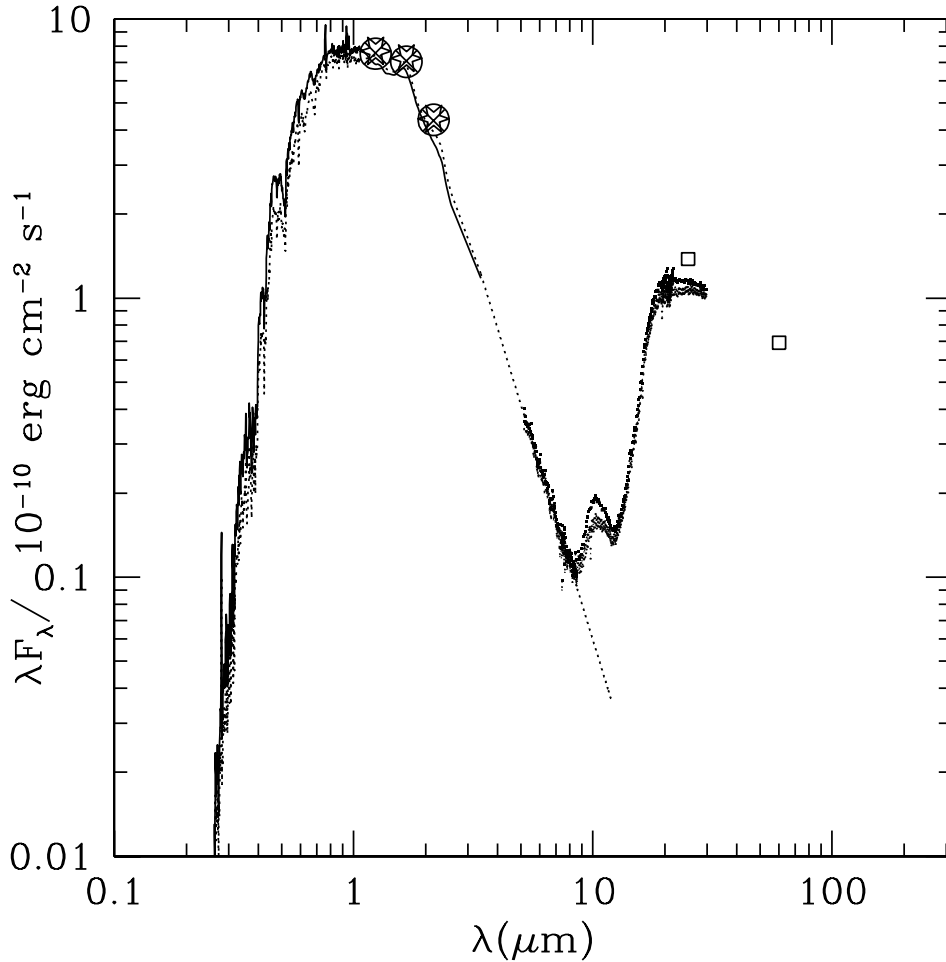


Fig. 3.— Combined spectrum of the central stars for a 4 *Myr* old binary system (solid line). The observed mid-IR SED of CoKu Tau/4 is corrected by four different extinction laws: Moneti et al. (2001) (upper curve), McClure (2009) (next curve), Draine (2003) (next curve) and Mathis (1990) (lower curve). The three last curves are very similar. IRAS data (Furlan et al. 2007) are represented by open squares, and the 2MASS data are crosses, circles and stars, corresponding to Mathis, Moneti and Draine extinction laws, respectively. The synthetic spectrum adopted in D05 is also plotted (dotted line).

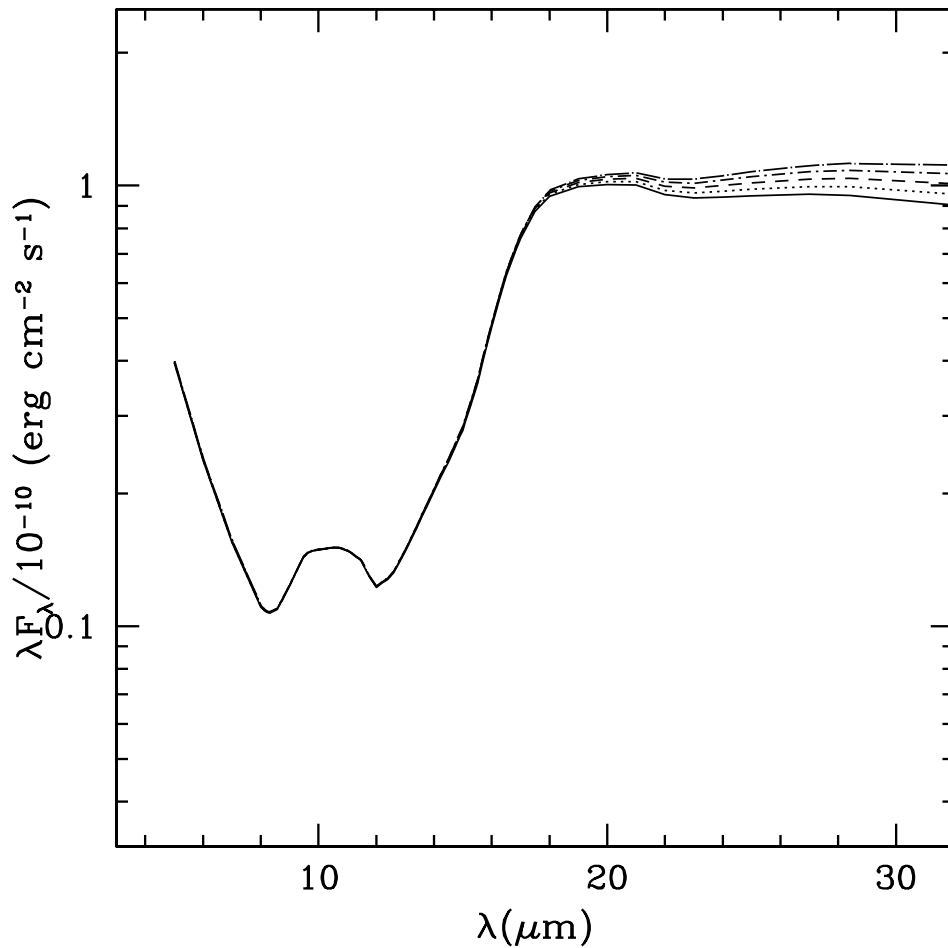


Fig. 4.— SEDs of non-axisymmetric models. The wall is an ellipse with a semiminor axis (b) along the line connecting both stars. The binary system has an age of 4 Myrs , with $\phi = 0.5, \alpha = 0, \cos i = 0.5$, and $h = 0.28a$. The models have $b = R_{cb} - 0.4a$ (solid); $b = R_{cb} - 0.3a$ (dotted); $b = R_{cb} - 0.2a$ (dashed); $b = R_{cb} - 0.1a$ (dot-dashed), and $b = R_{cb} - 0.0a$ (dot-long-dashed).

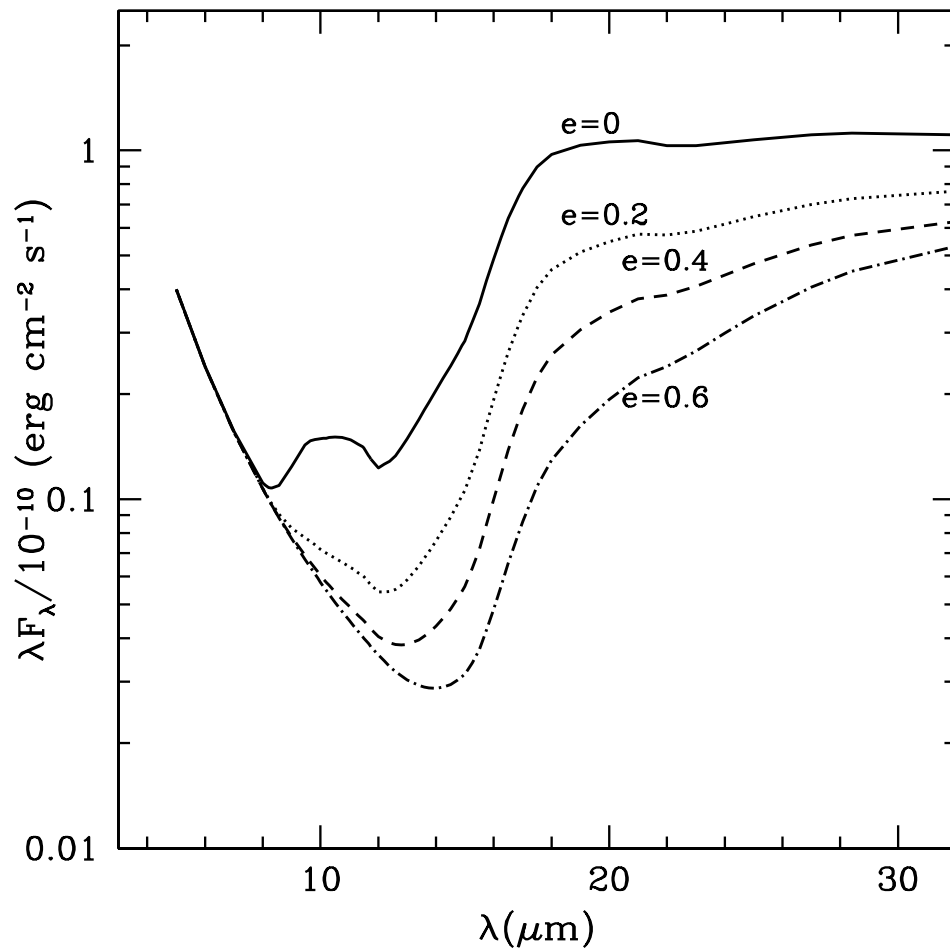


Fig. 5.— SEDs of models with different binary eccentricities and an age of 4 *Myrs*, with $\phi = 0.5, \alpha = 0, \cos i = 0.5$, and $h = 0.28a$. The parameters are given in Table 2 for each model; model E1 (solid); model E2 (pointed); model E3 (dashed); and model E4 (dot-dashed).

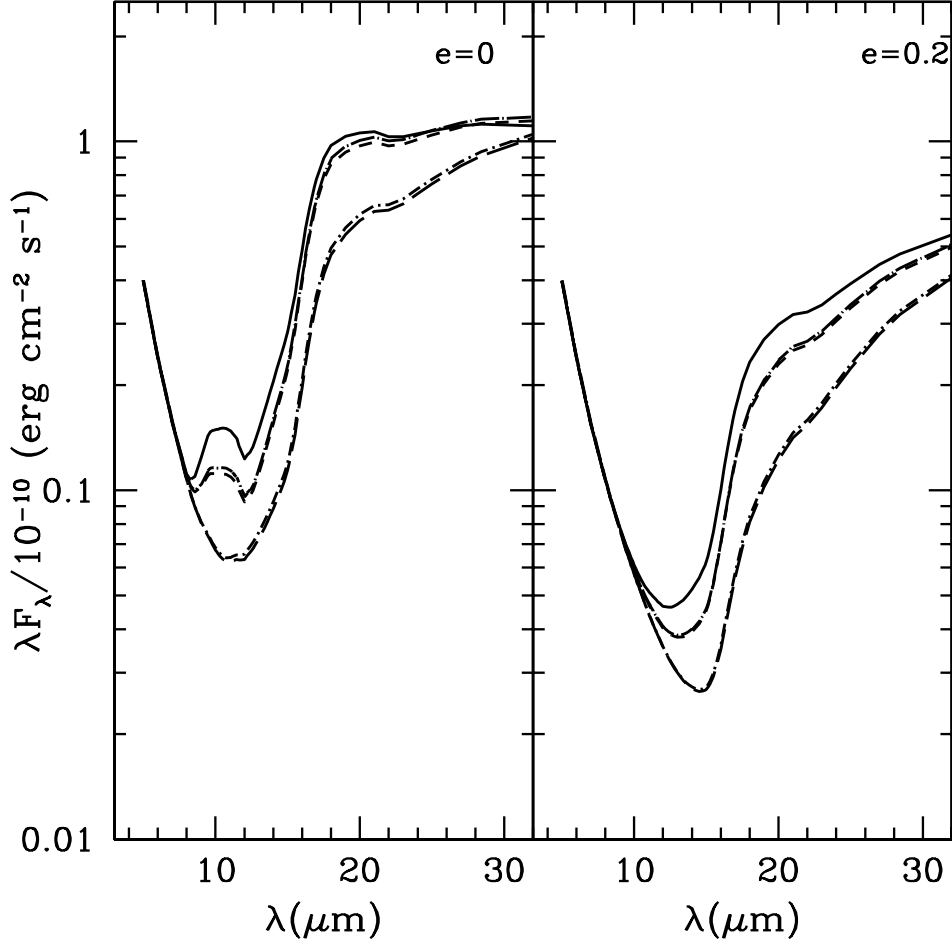


Fig. 6.— Variation of the synthetic SED with α for $e = 0$ (left plot) and $e = 0.2$ (right plot), with $\phi = 0.5, \cos i = 0.5$, and $h = 0.28a$. For the $e = 0$ case, the models are: E1, $\alpha = 0.0$ (solid), AE1, $\alpha = 0.25$ (small-dashed), AE2, $\alpha = 0.5$ (long-dashed), AE3, $\alpha = 1.5$ (dot-dashed) and AE4, $\alpha = 1.75$ (dot-long dashed). For the $e = 0.2$ case, the models are: AE5, $\alpha = 0.0$ (solid), AE6, $\alpha = 0.25$ (small-dashed), AE7, $\alpha = 0.5$ (long-dashed), AE8, $\alpha = 1.5$ (dot-dashed) and AE9, $\alpha = 1.75$ (dot-long dashed). See table 2 for more details about the models.

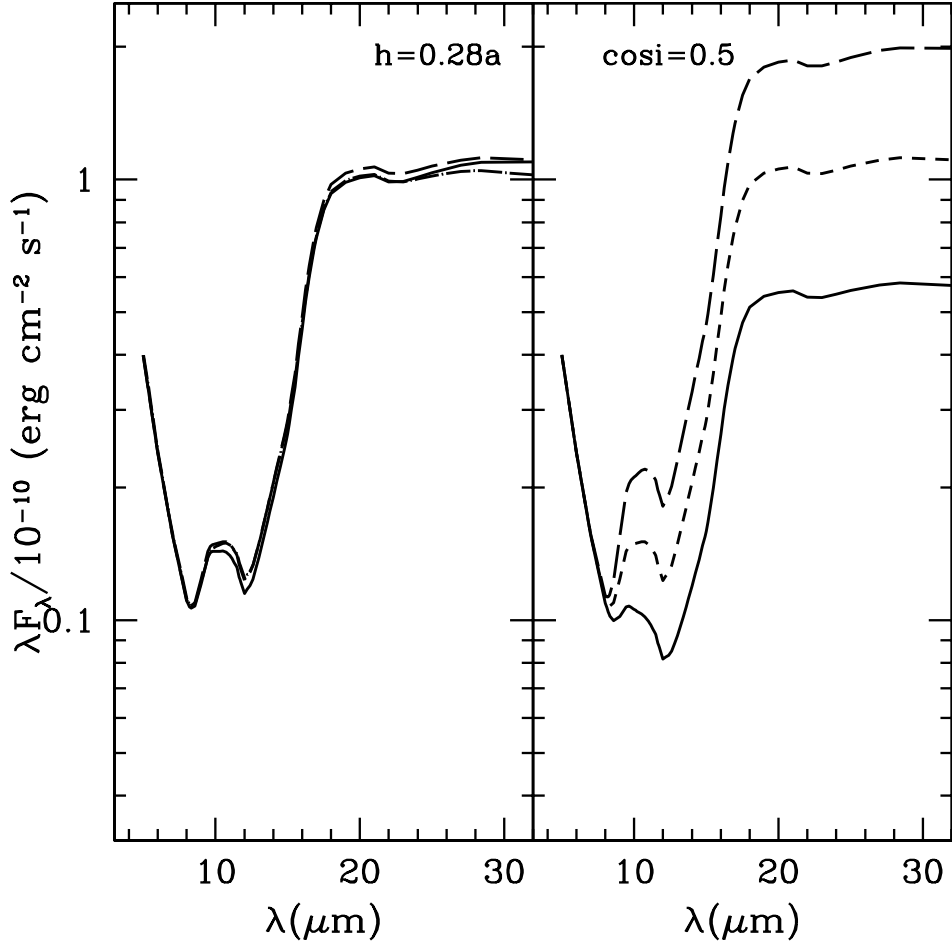


Fig. 7.— The left plot illustrates the dependence of the synthetic SED with inclination angle i , with $e = 0, \phi = 0.5, \alpha = 0, R_{cb} = 1.7a$. The plotted models are: IH1, $\cos i = 0.3$ (solid), E1, $\cos i = 0.5$ (long-dashed), and IH2, $\cos i = 0.7$ (dot-long-dashed). The right plot show models for various h with the same values for e, ϕ, α and R_{cb} . The models are: IH3, $h = 0.14$ (solid), E1, $h = 0.28$, (dashed) and IH4, $h = 0.56$ (long-dashed).

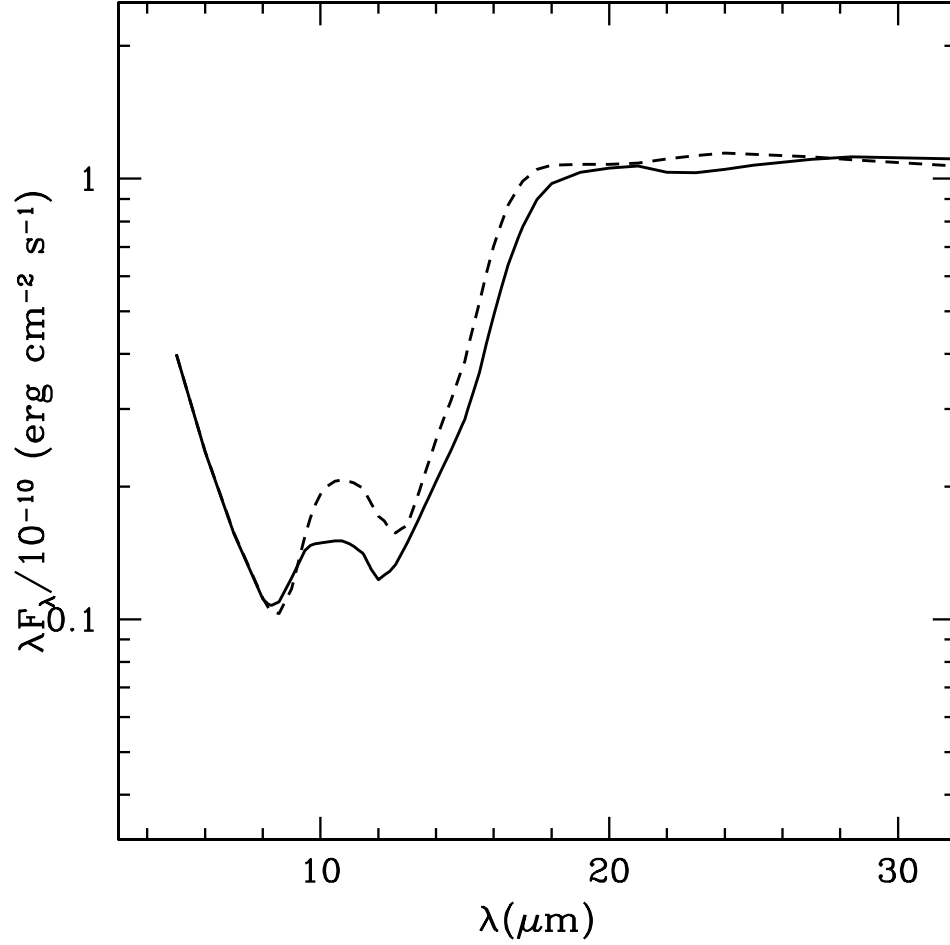


Fig. 8.— Change of the SED for the fiducial model (E1) for two silicates: pyroxene and olivines, with $e = 0, \phi = 0.5, \alpha = 0, \cos i = 0.5, R_{cb} = 1.7a$ and $h = 0.28a$. The solid line corresponds to pyroxenes (model E1), and the dashed line corresponds to olivines (model PO1).

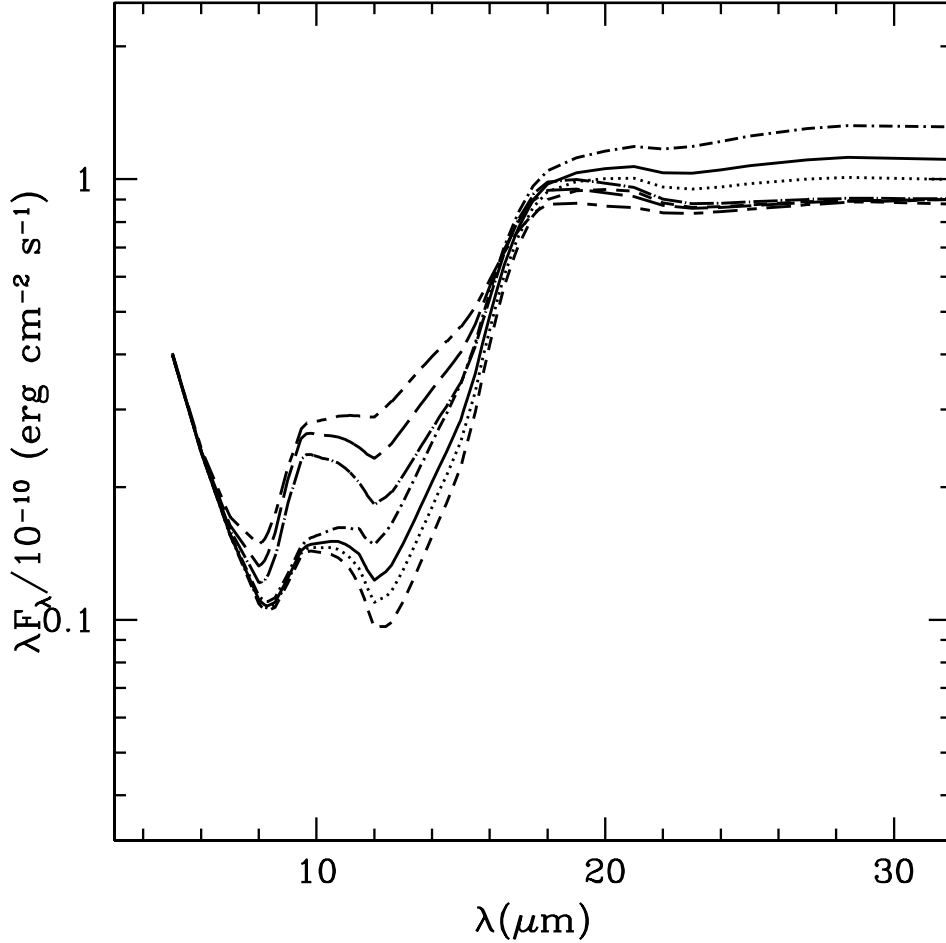


Fig. 9.— Change of the SED for the fiducial model (E1) for various carbon components, with $e = 0, \phi = 0.5, \alpha = 0, \cos i = 0.5, R_{cb} = 1.7a$ and $h = 0.28a$. The solid line corresponds to the fiducial model (E1, $\zeta_{grap} = 0.0025$), the dashed line corresponds to the model with zero graphite abundance (PA1), and the long-dashed curve shows the model with amorphous carbon instead of graphite with the same abundance (PA2). Also, we show cases with zero amorphous carbon abundance for $\zeta_{grap} = 0.00125$ (PA3,dotted), and for $\zeta_{grap} = 0.0050$ (PA4,dot-dashed). Other cases with zero graphite abundance include $\zeta_{am} = 0.00125$ (PA5,dot-long-dashed) and $\zeta_{am} = 0.0050$ (PA6,small-long-dashed).

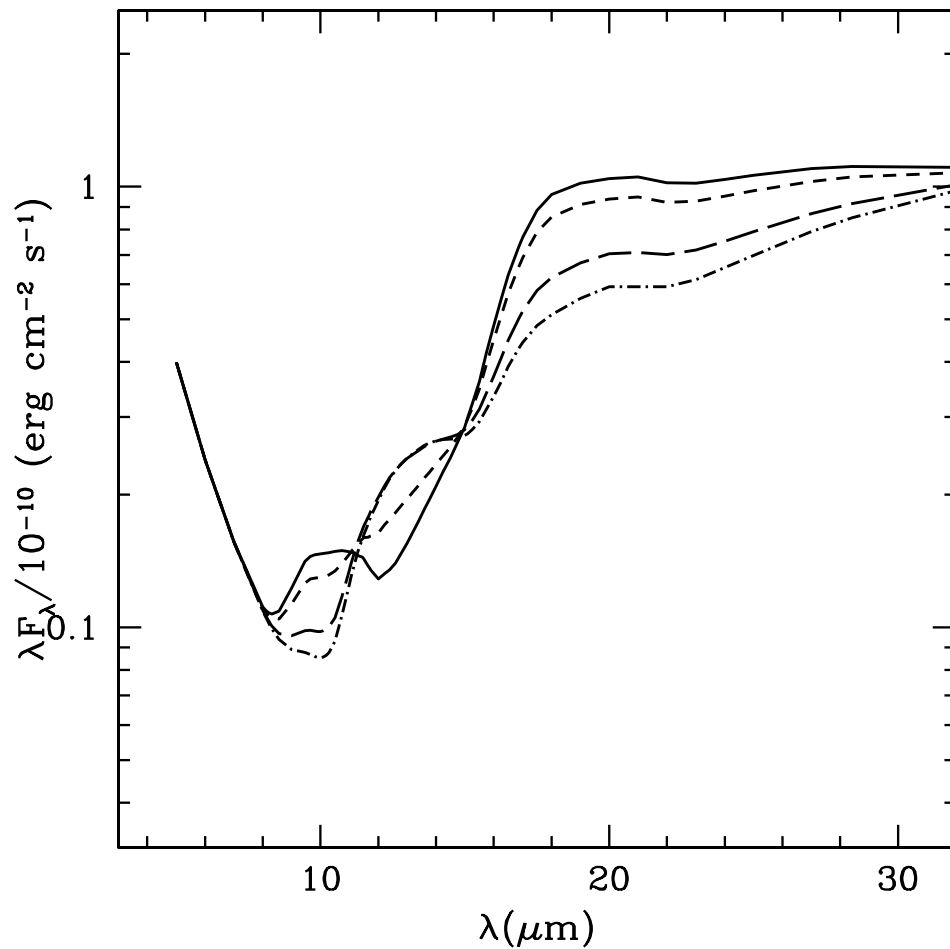


Fig. 10.— Change of the SED for the fiducial model (E1), including water ice, with $e = 0, \phi = 0.5, \alpha = 0, \cos i = 0.5, R_{cb} = 1.7a$ and $h = 0.28a$. The plotted models are $\zeta_{ice} = 0.000056$ (PI1, solid), $\zeta_{ice} = 0.00056$ (PI2, dashed), $\zeta_{ice} = 0.0028$ (PI3, long-dashed), and $\zeta_{ice} = 0.0056$ (PI4, dot-dashed).

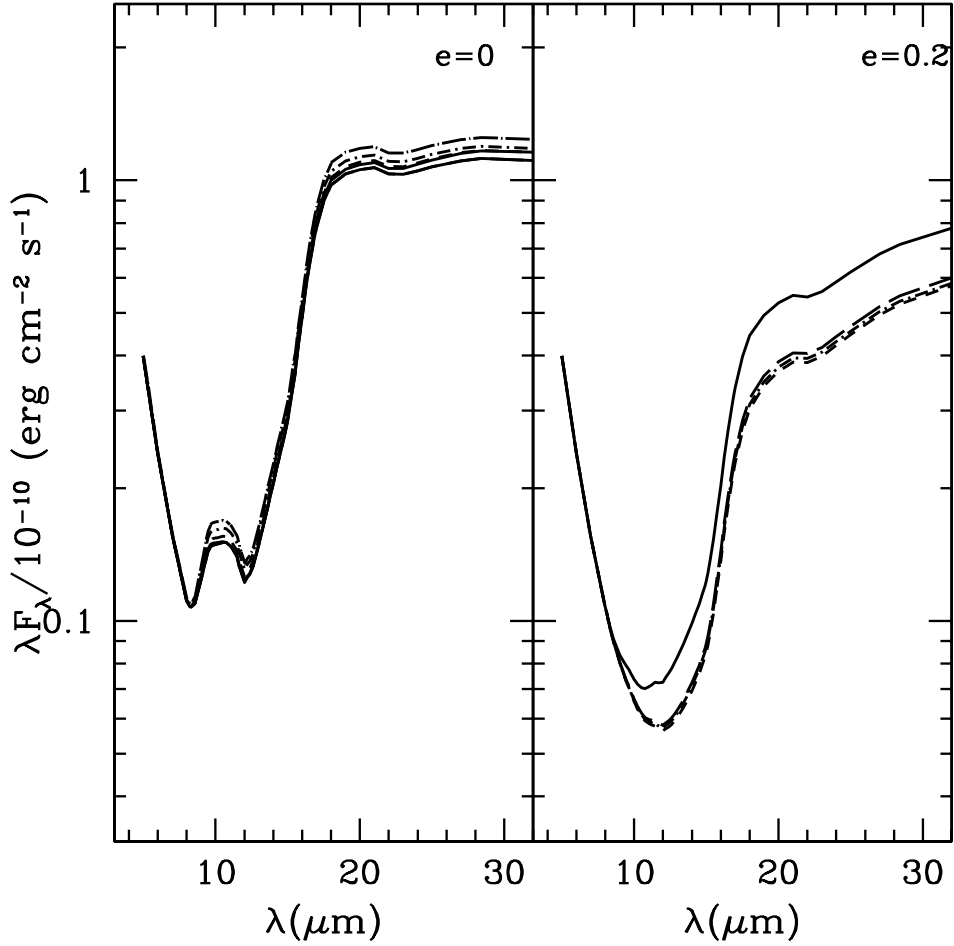


Fig. 11.— Time evolution of the synthetic SED of an $e = 0$ (left plot) and an $e = 0.2$ (right plot) system. For the $e = 0$ case, the plotted models are: PE1, $t = 0.0T/2$ (solid), PE2, $t = 0.25T/2$ (small-dashed), E1, $t = 0.5T/2$ (long-dashed), PE3, $t = 0.75T/2$ (dot-dashed), and PE4, $t = 1.0T/2$ (dot-long dashed). For the $e = 0.2$ case, the plotted models are: PE4, $t = 0.0T/2$ (solid), PE5, $t = 0.2T/2$ (small-dashed), PE6, $t = 0.45T/2$ (long-dashed), PE7, $t = 0.7T/2$ (dot-dashed), and PE8, $t = 0.9T/2$ (dot-long dashed). T is the orbital period. For both plots, $\alpha = 0, \cos i = 0.5$, and $h = 0.28a$

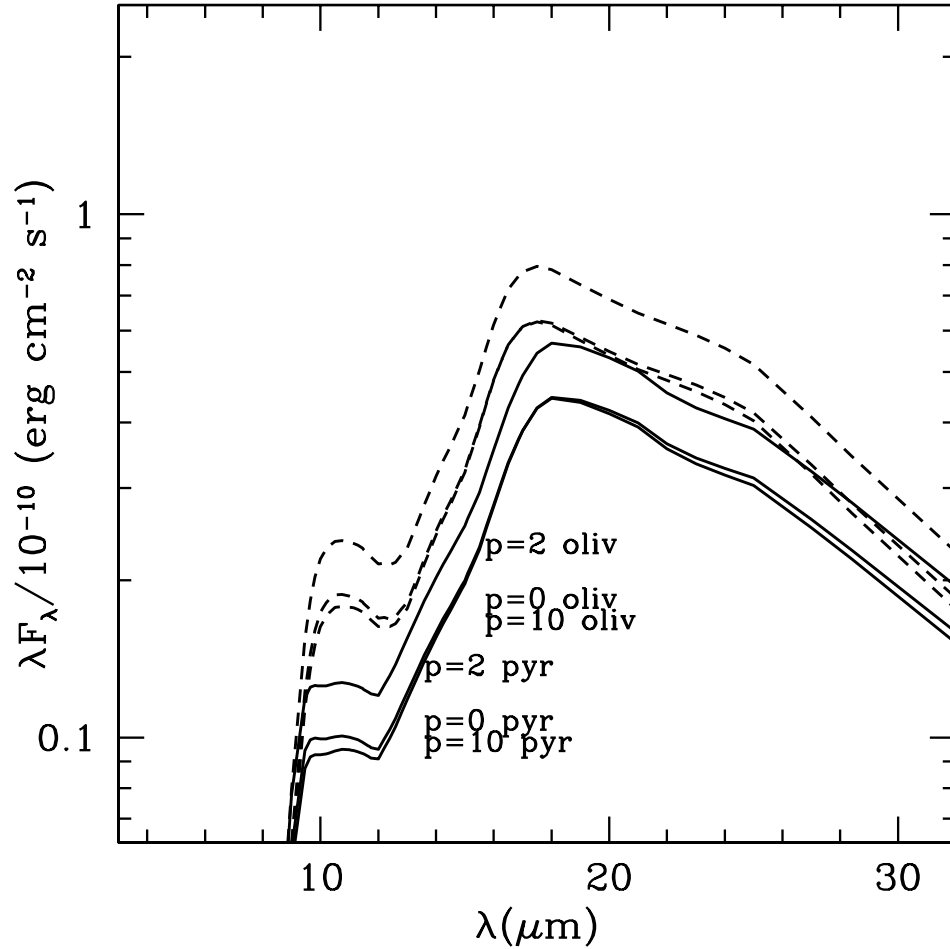


Fig. 12.— Emission of optically thin material in the disk hole of a 4 *Myrs* old binary system. Pyroxenes: $p = 0$ (middle), $p = 2$ (upper), $p = 10$ (lower), all solid lines. Olivines: $p = 0$ (middle), $p = 2$ (upper), $p = 10$ (lower), all dashed lines. For each case, the mass of dust in the hole is $1 \times 10^{-9} M_{\odot}$ and it is distributed between $R=1.4a$ and $R=1.7a$.

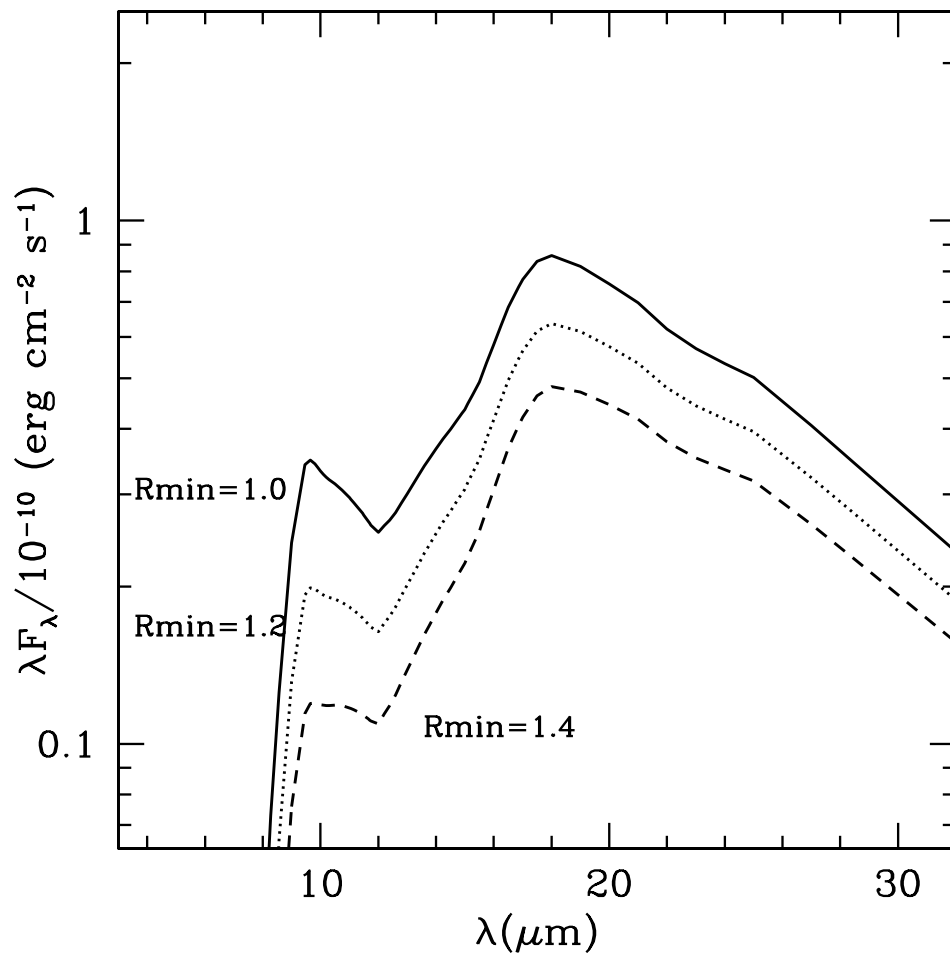


Fig. 13.— Emission of optically thin material in the disk hole of a 4 *Myrs* old binary system for various R_{min} . $R_{min} = 1.0a$ (solid), $R_{min} = 1.2a$ (dotted) and $R_{min} = 1.4a$ (dashed). For each case, the mass of dust in the hole is $8 \times 10^{-9}M_\odot$, $6.2 \times 10^{-9}M_\odot$ and $4.8 \times 10^{-9}M_\odot$ respectively, and it is distributed between $R = R_{min}$ and $R = 1.7a$.

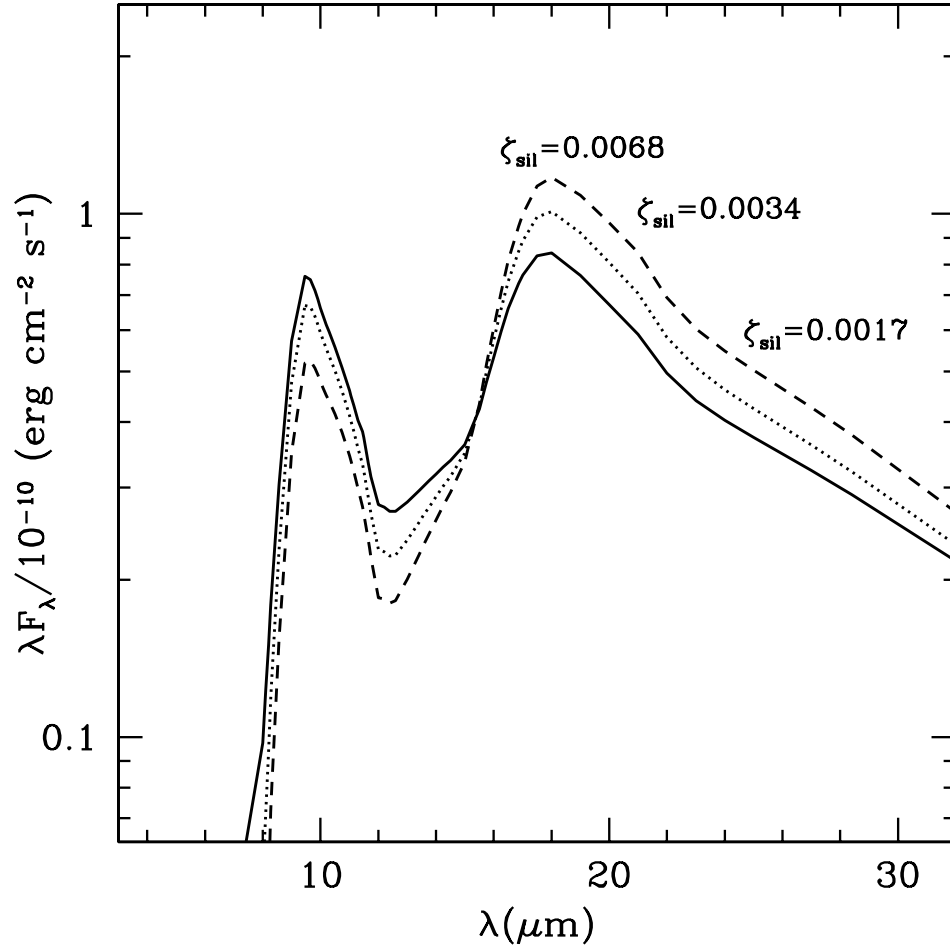


Fig. 14.— Emission of optically thin material in the disk hole of a 4 *Myrs* old binary system for various silicates abundances. $\zeta_{sil} = 0.0017$ (solid), $\zeta_{sil} = 0.0034$ (dotted) and $\zeta_{sil} = 0.0068$ (dashed). For each case, the mass of dust in the hole is distributed between $R=1.4a$ and $R=1.7a$.

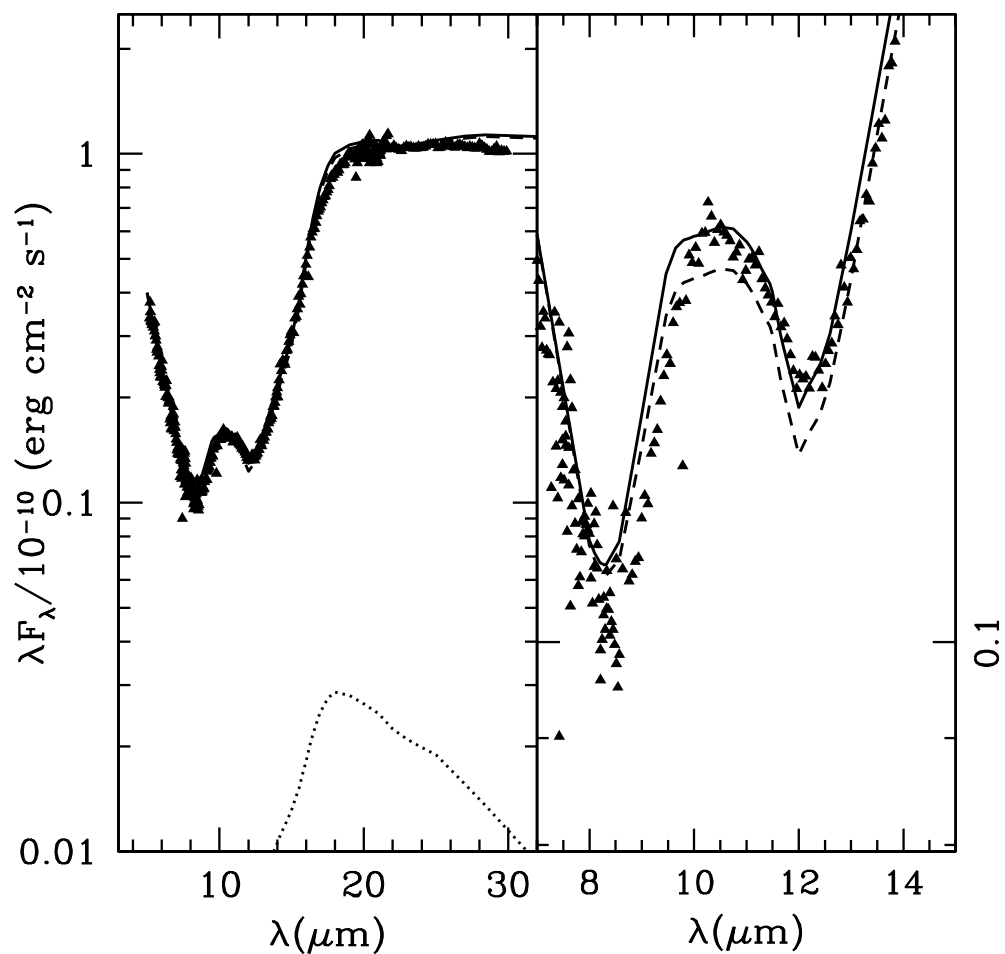


Fig. 15.— SED of model M1, with $e = 0$, age= 4 *Myrs* (see table 2) compared to the Spitzer IRS SED of CoKu Tau/4 (points), corrected with the reddening law of Draine (2003). We show the total SED (solid line), the contribution from the wall (dashed line) and from optically thin material in the hole (dotted line). The right plot shows the details of the 10 μm band.

Table 1. Stellar Parameters

spectral type	$M_*(M_\odot)$	$T_*(K)$	$R_*(R_\odot)$	$L_*(L_\odot)$
M1	0.5	3894	1.178	0.2886
M0	0.6	4027	1.261	0.3782

Table 2. Models discussed in this paper^a

Series	Figure	Model	$a(AU)$	e	$\phi(\pi)$	$\alpha(\pi)$	$\cos i$	$R_{cb}(a)$	$h(a)$	Dust ^b	T_{wall}
Ecc	5	E1	7.43	0	0.5	0	0.5	1.7	0.28	1	136.5
...	5	E2	9.287	0.2	0.5	0	0.5	2.35	0.28	1	110.7
...	5	E3	12.38	0.4	0.5	0	0.5	2.7	0.28	1	95.2
...	5	E4	18.575	0.6	0.5	0	0.5	2.95	0.28	1	80.7
α, ecc	6	AE1	9.40	0	0.5	0.25	0.5	1.7	0.28	1	125.0
...	6	AE2	14.87	0	0.5	0.5	0.5	1.7	0.28	1	103.0
...	6	AE3	14.87	0	0.5	1.5	0.5	1.7	0.28	1	103.8
...	6	AE4	9.40	0	0.5	1.75	0.5	1.7	0.28	1	125.6
...	6	AE5	9.29	0.2	0.5	0.0	0.5	2.9	0.28	1	99.60
...	6	AE6	11.75	0.2	0.5	0.25	0.5	2.9	0.28	1	91.21
...	6	AE7	18.58	0.2	0.5	0.5	0.5	2.9	0.28	1	77.12
...	6	AE8	18.58	0.2	0.5	1.5	0.5	2.9	0.28	1	77.44
...	6	AE9	11.75	0.2	0.5	1.75	0.5	2.9	0.28	1	91.47
i, h	7	IH1	7.43	0	0.5	0	0.3	1.7	0.28	1	136.1
...	7	IH2	7.43	0	0.5	0	0.7	1.7	0.28	1	136.7
...	7	IH3	7.43	0	0.5	0	0.5	1.7	0.14	1	136.9
...	7	IH4	7.43	0	0.5	0	0.5	1.7	0.56	1	135.2
pyr,oliv	8	PO1	7.43	0	0.5	0	0.5	1.7	0.28	1a	146.2
pyr,amorph	9	PA1	7.43	0	0.5	0	0.5	1.7	0.28	2	136.5
...	9	PA2	7.43	0	0.5	0	0.5	1.7	0.28	3	166.8
...	9	PA3	7.43	0	0.5	0	0.5	1.7	0.28	4	136.5
...	9	PA4	7.43	0	0.5	0	0.5	1.7	0.28	5	136.5
...	9	PA5	7.43	0	0.5	0	0.5	1.7	0.28	6	158.8
...	9	PA6	7.43	0	0.5	0	0.5	1.7	0.28	7	173.8
pyr,ice	10	PI1	7.43	0	0.5	0	0.5	1.7	0.28	8	136.2
...	10	PI2	7.43	0	0.5	0	0.5	1.7	0.28	9	134.0
...	10	PI3	7.43	0	0.5	0	0.5	1.7	0.28	10	128.3
...	10	PI4	7.43	0	0.5	0	0.5	1.7	0.28	11	125.1
t, ecc	11	PE1	7.43	0	0	0	0.5	1.7	0.28	1	135.8
...	11	PE2	7.43	0	0.25	0	0.5	1.7	0.28	1	136.7
...	11	PE3	7.43	0	0.75	0	0.5	1.7	0.28	1	137.3
...	11	PE4	7.43	0	1	0	0.5	1.7	0.28	1	137.9
...	11	PE5	9.29	0.2	0	0	0.5	2.9	0.28	1	112.7
...	11	PE6	9.29	0.2	0.5	0	0.5	2.9	0.28	1	108.3
...	11	PE7	9.29	0.2	1	0	0.5	2.9	0.28	1	108.9

Table 2—Continued

Series	Figure	Model	$a(AU)$	e	$\phi(\pi)$	$\alpha(\pi)$	$\cos i$	$R_{cb}(a)$	$h(a)$	Dust ^b	T_{wall}
...	11	PE8	9.29	0.2	1.5	0	0.5	2.9	0.28	1	108.7
CoKu Tau/4	15	M1	7.43	0	0.5	0	0.5	1.7	0.28	1	136.5

^aThe column titles are given as in the text.

^bThe numbers in the column “Dust” refer to different adopted abundances. See Table 3 for the dust abundances.

Table 3. Dust abundances

Dust model	ζ_{grap}	ζ_{sil}	ζ_{troi}	ζ_{ice}	ζ_{amorp}	wall sil ^a
1	0.0025	0.0034	7.68E-4	0.0	0.0	pyr
1a	0.0025	0.0034	7.68E-4	0.0	0.0	oliv
2	0.0	0.0034	7.68E-4	0.0	0.0	pyr
3	0.0	0.0034	7.68E-4	0.0	0.0025	pyr
4	0.00125	0.0034	7.68E-4	0.0	0.0	pyr
5	0.005	0.0034	7.68E-4	0.0	0.0	pyr
6	0.0	0.0034	7.68E-4	0.0	0.00125	pyr
7	0.0	0.0034	7.68E-4	0.0	0.005	pyr
8	0.0025	0.0034	7.68E-4	5.6E-5	0.0	pyr
9	0.0025	0.0034	7.68E-4	5.6E-4	0.0	pyr
10	0.0025	0.0034	7.68E-4	2.8E-3	0.0	pyr
11	0.0025	0.0034	7.68E-4	0.0056	0.0	pyr

^a”Wall sil” refers to the type of silicates used in the wall.